Journal of Materials Chemistry A

ROYAL SOCIETY OF CHEMISTRY

REVIEW

View Article Online
View Journal | View Issue

Cite this: J. Mater. Chem. A, 2025, 13, 29688

Advancing the synthesis strategy and interface modification for efficient perovskite quantum dot solar cells

Yuanze Xu, [a] Xiaoyu Zhang, [a] Chenwei Zhu [b] and Qiuming Yu *[a]

Perovskite quantum dots (PeQDs) have emerged as a promising material for photovoltaics due to their facile synthesis, tunable bandgap, high absorption coefficient, and defect tolerance. Owing to their superior optoelectronic properties, perovskite quantum dot solar cells (PeQDSCs) have achieved a certified power conversion efficiency (PCE) of 18.1%, surpassing that of colloidal quantum dot solar cells. To further improve the device performance and stability of PeQDSCs, we need deeper mechanistic insights into material chemistry and may need to develop new synthesis strategies and ligand chemistry. In this review, we discuss challenges, current progress and future directions of PeQDSCs from a chemical perspective. We first introduce the unique chemical and optoelectronic properties of PeQDs and outline current challenges of PeQDSCs. We then review recent advances in PeQD synthesis, including hot injection synthesis, post-synthesis purification, and composition engineering. Moreover, we discuss the surface ligand chemistry for solid-state PeQD films, ranging from the ligand exchange reaction, the soaking reaction, processing solvent engineering, and conductive PeQD ink synthesis to nanocomposite formulation. Lastly, we propose future research directions with a goal of large-area, flexible and tandem solar cells.

Received 19th May 2025
Accepted 30th July 2025

DOI: 10.1039/d5ta03996g

rsc.li/materials-a

1. Introduction

Metal halide perovskites (MHPs) have emerged as highly promising optoelectronic materials due to their superior optoelectronic properties and low-cost solution processability.[1–3] The power conversion efficiencies (PCEs) of perovskite solar cells have reached up to 27.3%,[4] rivaling those of silicon-based solar cells. The high cell performance stems from long carrier lifetime, moderate carrier mobility, tunable band structures, and low exciton binding energy.[5–8] However, polycrystalline MHP films suffer from poor phase stability under external stresses, such as light, heat and humidity, and challenges in scalable fabrication.[9,10] These limitations hinder the wide commercialization of perovskite solar cells and have prompted exploration of alternative material structures and processing techniques.

One of the most promising alternatives to bulk polycrystalline MHPs is perovskite quantum dots (PeQDs). As illustrated in Fig. 1a, the MHP crystal lattice structure features a three-dimensional network of corner-sharing $[MX_6]^{4-}$ octahedra (where M = Pb or Sn, X = Cl, Br, or I), with the interstitial cavities occupied by A-site cations, such as Cs^+, methylammonium (MA^+), or formamidinium (FA^+). As the nanocrystalline form of MHPs, PeQDs consist of a MHP crystal core and an organic ligand shell wrapped around the core. PeQDs exhibit strong defect tolerance and robust long-term stability.[11,12] Furthermore, PeQDs significantly extend the tunability of MHPs in both chemical compositions and electronic structures with facile synthesis.[13,14] From a fabrication standpoint, PeQDs offer significant technical advantages for scalable production. Unlike bulk MHP films, where crystallization and film formation occur concurrently, PeQD synthesis decouples crystallization from film deposition. This separation enables independent optimization of crystal quality and film formation, allowing for various deposition techniques including inkjet printing, slot-die coating, or spraying.[15–17] Due to these advantages, PeQD solar cells (PeQDSCs) can easily adopt both n–i–p conventional and p–i–n inverted device architectures (Fig. 1b) and have demonstrated great potential in cell performance. As shown in Fig. 1c, since the first PeQDSC was demonstrated in 2016,[18] the PCE of PeQDSCs has steadily improved. The PCE of PeQDSCs surpassed that of conventional colloidal quantum dot solar cells by 2017 (ref. 19) and reached 18.1% to date.[20] More than half of the studies on PeQDSCs were dedicated to all-inorganic PeQDs, specifically $CsPbI_3$ QDs, for the well-established high temperature synthesis and structural integrity by less mobile surfaces. Recently, organic cation and mixed cation PeQDSCs have demonstrated higher potential for PCEs due to their more favorable band structure. Although significant improvements in PCEs have been realized over the past decade through compositional tuning and chemical modification, there

[a]Robert Frederick Smith School of Chemical and Biomolecular Engineering, Cornell University, Ithaca, New York 14853, USA. E-mail: qy10@cornell.edu
[b]Department of Materials Science and Engineering, Cornell University, Ithaca, New York 14853, USA

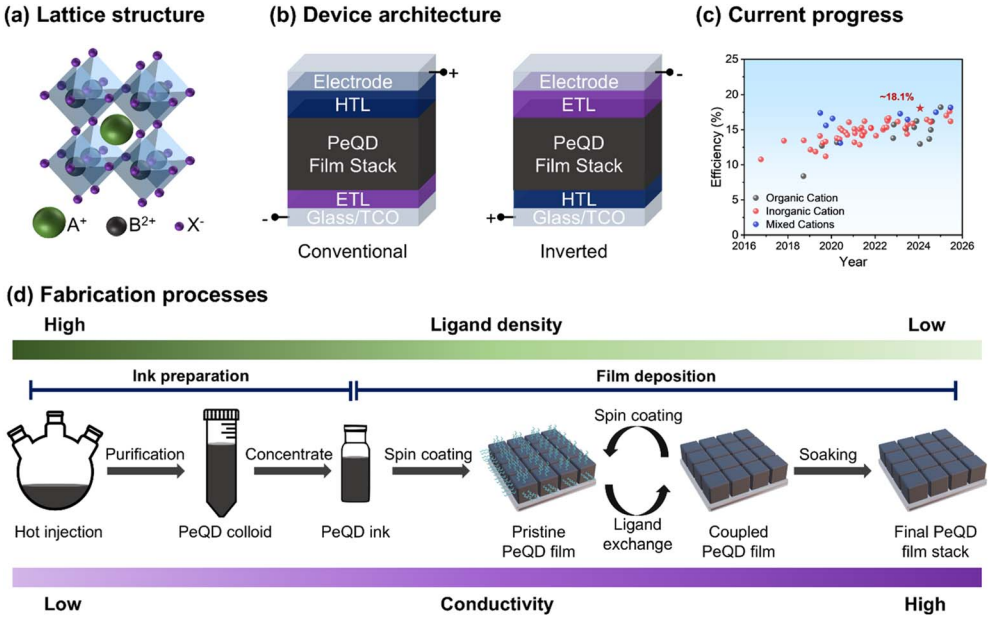

Fig. 1 (a) Schematic illustration of a metal halide perovskite lattice. (b) The conventional and inverted device architecture of PeQDSCs. (c) Recent progress in PeQDSC power conversion efficiencies (PCEs). (d) Fabrication processes of PeQDSCs and the change in ligand density and conductivity during the processes.

remains a noticeable gap when compared to the state-of-the-art cell performance of bulk thin film perovskite solar cells.

The fabrication process of PeQD films involves two stages: (1) PeQD ink preparation and (2) PeQD film deposition (Fig. 1d). PeQDs are usually synthesized *via* hot-injection methods due to their excellent control in PeQD size and size distribution.[21] The crude PeQDs then undergo purification steps by sequential centrifugation and redispersion of PeQD pellets, where the unreacted precursors and excess ligands are decanted. The PeQD colloids after purification are concentrated into high density PeQD inks for deposition. During the deposition stage, PeQD inks are spin coated into solid-state PeQD films, where the PeQDs are often randomly stacked with their pristine ligand shell. Due to the insulating nature of native long-chain ligands, a ligand exchange step needs to be conducted to replace them with short-chain conductive ligands. The PeQD films are subjected to antisolvent treatment for the native ligands to dissociate. This spin coating and ligand exchange cycle is repeated 3–5 times to stack solid-state PeQD films of 300–500 nm thickness. After thick PeQD films are obtained, the films are soaked in a solution, often with ionic salts, to further enhance the electronic coupling between PeQDs. The performance of PeQDSCs was significantly improved through chemical modifications to the fabrication process. During the fabrication process, every time the solid-state PeQD films are subjected to antisolvent treatment, the ligand density will drop and the film conductivity will increase. The drop in ligand density mobilizes surface species of PeQDs and reduces the activation energy of surface defects. Therefore, defect control is crucial for each step of PeQDSC fabrication. Moreover, PeQD composition shapes the electronic band structure and alters the optoelectronic properties of PeQD films. It is therefore critical for charge carrier dynamics and needs to be rationally designed. By advancing the synthesis strategies and surface modification methods of PeQDs, PeQDSCs can reach their full commercial potential.

This review, from a chemical perspective, summarizes recent strategies and advances in improving the performance and stability of PeQDSCs. An overview of the key chemical and optoelectronic properties of PeQDs will be provided, including the facile composition tunability of individual PeQDs and the unique charge carrier dynamics in PeQD films. Representative approaches to improving the synthesis of PeQDs are then discussed, covering two synthesis methods based on precursor types, post-synthesis purification for surface ligand management and vacancy filling and cation-exchange reactions for composition engineering. The following section delves into the process conditions and underlying mechanisms involved in PeQD film fabrication, including the mechanisms of structural changes and electronic coupling of PeQDs induced by ligand exchange under antisolvent treatment and its variations. The impact of post-deposition soaking on charge collection efficiency in PeQDSCs is explained. Furthermore, conductive PeQD inks, ionically stabilized or at a metastable state, can suppress defect formation and simplify the fabrication process. Finally, future research directions are proposed for both synthetic methods of PeQD inks and the design of PeQDSC device architectures. Advancements in PeQD ink chemistry may further enable large-area, flexible, and tandem solar cell applications.

2. Unique structural and electronic properties of PeQDs

PeQDs feature a unique structure that defines their optoelectronic properties. PeQDs consist of a nanocrystalline MHP core,

typically 2–20 nm in size, with a shell of long-chain aliphatic ligands. When the core size shrinks below the Bohr radius, it enters the quantum confinement regime, resulting in a size-dependent electronic structure where smaller PeQDs show larger bandgaps. This confinement increases exciton binding energy and enables near-unity photoluminescence quantum yield (PLQY). Additionally, the ligand shell plays a critical role by solubilizing MHP precursors, controlling core growth, stabilizing colloids, and passivating surface defects.

2.1. Structural versatility and stability

Bulk MHP materials suffer from various stability issues, including ion migration, ion segregation, phase transitions, and light-induced degradation. In contrast, PeQDs offer enhanced structural stability due to their nanoscale core size and the protective barrier provided by surface ligands. Additionally, PeQD composition can be easily tuned in the solution phase at room temperature, significantly expanding the compositional engineering window for MHP materials.

Since the valence and conduction band edges of MHP materials are determined by the bonding between the metal and halogen ions, the MHP lattice compositions are therefore critical in controlling the electronic band structure of MHP materials. Although a MHP lattice may adopt a wide range of halide compositions, bulk MHP films face severe halide migration and segregation issues.[22–25] Due to the soft ionic nature of the MHP lattice, the energy barrier for halides to migrate is low.[26,27] Under light illumination, halides migrate within and across crystal grains to segregate. Halide segregation can cause MHPs to deviate from the desired optoelectronic properties, hence hampering device performance. Halide migration out of the MHP lattice will cause structural collapse due to loss of halides, deteriorating the long-term device stability. For PeQDs, the ligand shell acts as a barrier against halide migration and largely alleviates the halide migration issue. Specifically, oleates bond strongly to surface halide vacancies and effectively block the halide migration channels *via* Schottky defects. The steric effect of long-chain aliphatic ligands also prevents the halide from hopping across PeQD surfaces. Therefore, the unique PeQD structure enables a continuously tunable halide composition with long-term stability. The halide compositions of PeQDs are readily tunable after synthesis without compromising the PeQD stability and PLQY. A fast anion exchange method was proposed using PbX_2 and alkylammonium halides as the halide sources (Fig. 2a).[28,29] These halide sources were mixed with PeQD colloids at room temperature to finish the reaction. The halide ions traveled between PeQD cores and halide sources in the liquid medium. As shown in Fig. 2b, by tuning the halide compositions, PeQDs were successfully synthesized with the emission peaks spanning the whole visible spectrum.

The A-site cation composition of the MHP lattice is critical in determining the electronic properties and phase stability. For a MHP composition to form the desired crystal phase, the Goldschmidt tolerance factor (t), as a function of the A-/B-/X-site ion radii, needs to fall between 0.85 and 1.[30] A t value outside

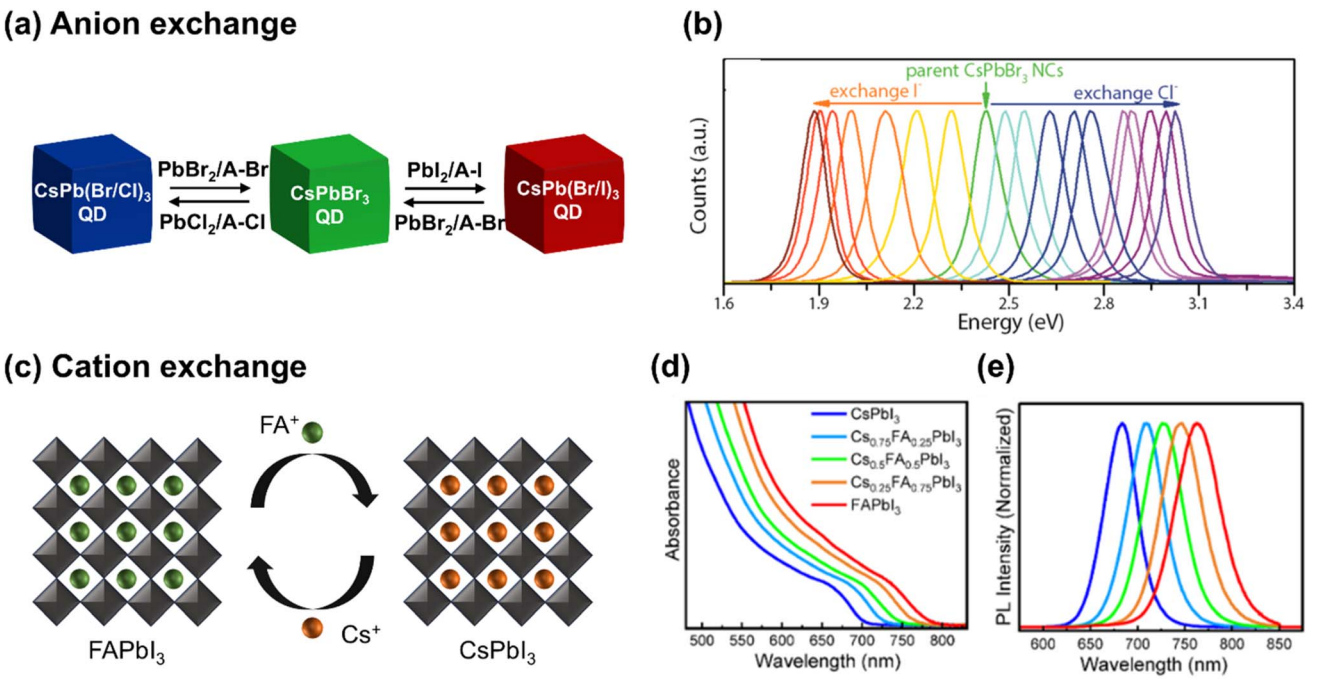

Fig. 2 Facile composition tuning of PeQDs. (a) Post-synthesis anion-exchange reaction with PbX_2 and alkylammonium halides as the halide sources to obtain $CsPbX_3$ PeQDs. (b) PL spectra of anion-exchanged $CsPbBr_3$ QDs spanning across the visible spectrum. Reproduced with permission from ref. 29. Copyright 2015 American Chemical Society. (c) Cation-exchange reaction between $FAPbI_3$ and $CsPbI_3$ QDs to obtain $FA_{1-X}Cs_XPbI_3$ QDs. (d) UV-vis and (e) PL spectra of $FA_{1-X}Cs_XPbI_3$ QDs obtained *via* the cation-exchange reaction. Reproduced with permission from ref. 35. Copyright 2018 American Chemical Society.

this range will cause severe lattice distortion and a subsequent phase transition to non-photoactive phases. However, even though the expected t value falls within this range, bulk MHP films may not form the desired crystal phase with any compositions. For example, attempts to spin coat MHP films with a high Cs ratio will face both low solubility of the CsI precursor and segregation of Cs at the top of the film due to crystallization kinetics.[31] When MHP crystal size shrinks, the surface energy contributes more to the Gibbs free energy profile and changes the photoactive phase of MHPs from kinetically trapped to thermodynamically favorable.[32,33] The lattice parameter induced microstrain can relax at the PeQD grain boundaries. Additionally, the gaps between PeQDs in solid-state PeQD films provide buffer space to help withstand thermal expansion. Therefore, PeQDs can stabilize the crystal phase for any arbitrary $FA_{1-x}Cs_xPbI_3$ compositions. $FA_{1-x}Cs_xPbI_3$ QDs can be synthesized *via* multiple cation-exchange reactions, which will be discussed in the next section. Continuously adding FA in the cation composition of $FA_{1-x}Cs_xPbI_3$ QDs will cause the lattice to distort from an orthorhombic γ-phase for $CsPbI_3$ to a cubic α-phase for $FAPbI_3$.[34] $FA_{1-x}Cs_xPbI_3$ QDs can be synthesized by the cation exchange reaction when intermixing $FAPbI_3$ and $CsPbI_3$ QDs (Fig. 2c), which will be discussed in detail in the following section. As shown in Fig. 2d and e, the absorption band edge and the emission peak of the $FA_{1-x}Cs_xPbI_3$ QDs can be continuously tuned by adjusting the ratio between the $CsPbI_3$ and $FAPbI_3$ QD colloids.[35]

2.2. Charge carrier dynamics of PeQD thin films

Solid-state PeQD films exhibit intriguing charge carrier dynamics by the interplay between quantum confinement, ligand effect and QD–QD interactions. Harnessing the charge carrier dynamics is critical in achieving high performance PeQDSCs. To construct PeQDSCs, a ligand exchange step is crucial to enhance the conductivity of PeQD films. During the ligand exchange, the QD–QD distance is reduced by replacing native long-chain ligands with short-chain ligands. This change in the microstructure reduces the dielectric barrier between PeQDs, allowing the wavefunction of individual PeQDs to extend across multiple PeQDs. In other words, the ligand exchange of PeQD films switches the state of PeQD films from dielectrically separated into electronically coupled. The primary photoexcitation species in the solid-state PeQD film change from polaronic excitons to large polarons.[36] The photogenerated charge carriers then favor dissociation over recombination. The dissociated charge carriers have less chance to recombine, leading to longer carrier diffusion length (Fig. 3a). This change in primary carriers contributes to more efficient charge transport across the PeQD films and charge collection of PeQDSCs.

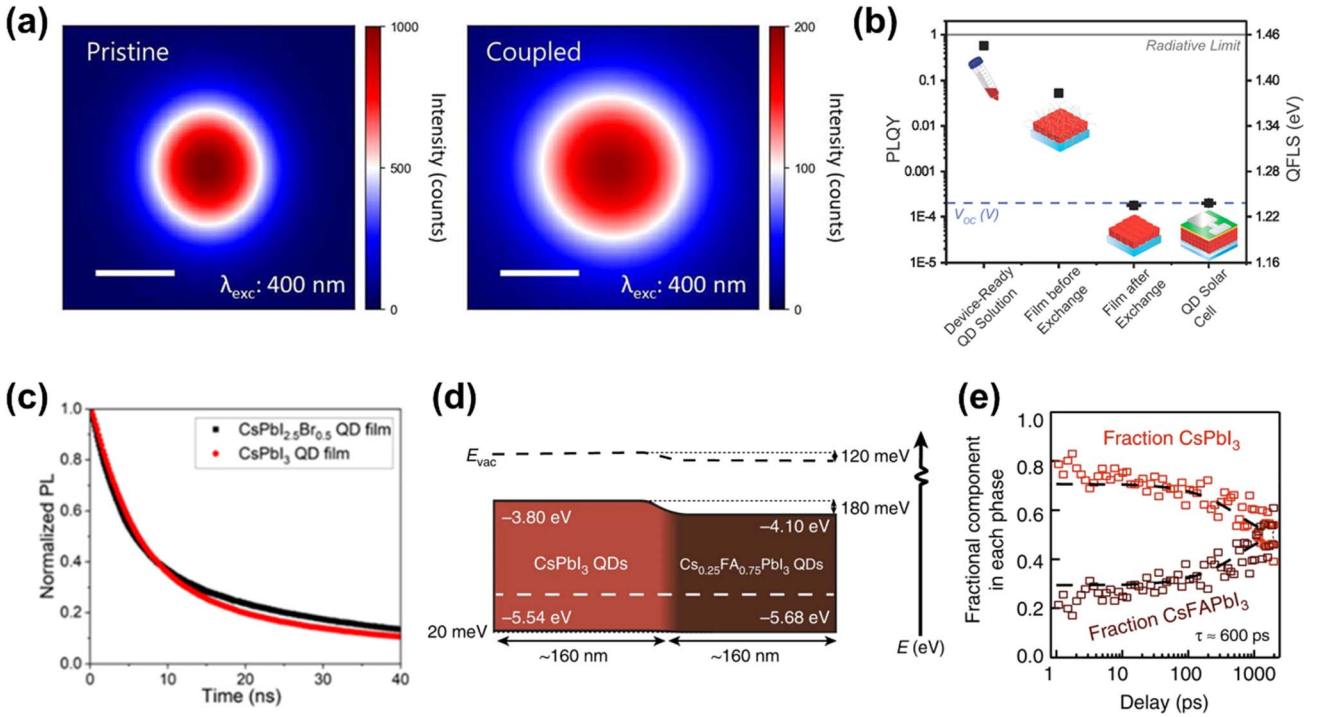

Fig. 3 Charge carrier dynamics of PeQD films. (a) Charge carrier diffusion length in pristine and coupled PeQD films obtained by spatially resolved photoluminescence. Reproduced with permission from ref. 36. Copyright 2023 American Chemical Society. (b) Evolution of PLQY at each step of the PeQDSC fabrication process. Reproduced with permission from ref. 39. Copyright 2023 American Chemical Society. (c) TRPL spectra of small $CsPbI_3$ QD films and large $CsPbI_{2.5}Br_{0.5}$ QD films. Reproduced with permission from ref. 40. Copyright 2024 American Chemical Society. (d) Schematic illustration of charge separation junctions between $CsPbI_3$ QD and $Cs_{0.25}FA_{0.75}PbI_3$ QD films. (e) Decomposed fraction of the transient absorption signals corresponding to $CsPbI_3$ QD and $Cs_{0.25}FA_{0.75}PbI_3$ QD films at each delay time. Reproduced with permission from ref. 41. Copyright 2019 under exclusive license to Springer Nature Limited.

A notable attribute of PeQDs is their near-unity PLQY, which originates from the combined effect of the intrinsic defect tolerance of the MHP lattice and the effective passivation from the ligand shell. PLQY directly leads to quasi-fermi level splitting (QFLS), which then determines the open-circuit voltage (V_{OC}) of PeQDSCs.[37,38] Thanks to the high PLQY, PeQDSCs reproducibly exhibit low V_{OC} losses. The high PLQY of PeQDs is a result of high crystal quality and ligand passivation from highly reproducible hot injection synthesis. Wieliczka *et al.* pointed out that unlike bulk MHPs, the V_{OC} of PeQDSCs is not limited by interface recombination that occurs at the perovskite active layer and the charge transport layers, but rather limited by the reduction of PLQY during the ligand exchange process (Fig. 3b).[39] Ligand exchange induces surface trap state formation and increases the background charge carrier concentration of PeQD films to even higher than that of bulk MHP films. They further showed that $FA_{1-X}Cs_XPbI_3$ QDs form shallow electronic traps with lower density compared to both $CsPbI_3$ and $FAPbI_3$ compositions, making it a more promising composition for PeQDSCs. Overall, the ligand exchange step is crucial in controlling the charge carrier dynamics of PeQD films, and in-depth understandings are required to further improve PeQDSC performance.

The extensive structure tunability of PeQDs provides multiple approaches to shape the electronic band structure. For example, to enlarge the bandgap of PeQDs, we can either enhance the quantum confinement by shrinking PeQD size or alter the halide-lead bonding by introducing more bromide. However, these structural changes result in different charge carrier dynamics. Hu *et al.* explored the underlying mechanisms of the PeQD band structure.[40] They synthesized small $CsPbI_3$ QDs and large $CsPbI_{2.5}Br_{0.5}$ QDs have an identical 1.85 eV bandgap. As shown in Fig. 3c, time-resolved photoluminescence (TRPL) spectra showed that small $CsPbI_3$ QDs exhibit a slower carrier recombination rate and faster carrier transfer rate than large $CsPbI_{2.5}Br_{0.5}$ QDs, indicating less non-radiative recombination and more efficient charge transport in $CsPbI_3$ QD films. Ultraviolet photoelectron spectrum (UPS) spectra showed that small $CsPbI_3$ QDs have more downshifted Fermi levels than large $CsPbI_{2.5}Br_{0.5}$ QDs, while both valence band maximum (VBM) and conduction band minimum (CBM) levels are similar among these two types of PeQDs. Therefore, the small $CsPbI_3$ QDs adopt a more intrinsic band structure. As a result, the $CsPbI_3$ QDs exhibit higher PCEs than $CsPbI_{2.5}Br_{0.5}$ QDs, owing to coherent lattice structures, suppressed defect density, and faster carrier transfer.

Due to the facile composition tuning and processing versatility, heterojunctions can be constructed within PeQD films for more favorable charge carrier dynamics. PeQDs with different band structures can be stacked sequentially to form a cascading band alignment, which favors charge separation at the junction interface and charge transport towards the charge selective layers.[41,42] As shown in Fig. 3d, $CsPbI_3$ QDs have a higher CBM than $Cs_{0.25}FA_{0.75}PbI_3$ QDs. Photogenerated charge carriers tend to separate at the interface between the two types of PeQD films, and electrons will transfer across the $Cs_{0.25}FA_{0.75}PbI_3$ QD film. Fig. 3e depicts the fraction of the transient absorption (TA) signal corresponding to each PeQD film. The excitation laser is incident on the $CsPbI_3$ QD film and creates a population of charge carriers. These carriers then transfer to the $Cs_{0.25}FA_{0.75}PbI_3$ QD film due to the band alignment, evidenced by the increase of the $Cs_{0.25}FA_{0.75}PbI_3$ phase fraction in the ground state bleaching signals with the probe delay time. We note that the dielectric confinement blocks the cation Cs^+ and FA^+ migration across the film, preventing the PeQD composition from homogenizing under light and bias. In light of these findings, PeQD core composition, crystal size, ligand shell and high order structures need to be synergistically designed in order to achieve ideal charge carrier dynamics.

3. Advanced synthesis of PeQDs

This section reviews advanced synthetic strategies for PeQDs optimized for high-performance photovoltaics. The predominant method employed is hot injection synthesis, which facilitates the synthesis of PeQDs with exceptional crystallinity, narrow size distributions, and near-unity PLQY. Post-synthesis, crude PeQD products require thorough purification to remove unreacted precursors, byproducts, and excess ligands, thereby enhancing their optoelectronic properties. Furthermore, composition engineering is leveraged to fine-tune the bandgap and improve phase stability by adjusting the ratios of A-, B-, and X-site ions. Collectively, these advanced synthetic techniques underpin the development of PeQDs with optimized performance and stability for next-generation solar cell applications.

3.1. Hot injection synthesis of PeQDs

The synthesis of PeQDs for photovoltaic applications mainly adopts the hot injection method due to its excellent control over the size, shape and composition. The as-synthesized PeQDs show well-defined shapes, narrow size distributions, and high PLQYs.[11,13] Based on different precursor selections, there are two types of hot injection synthesis methods for PeQDs, the binary precursor method and the ternary precursor method (Fig. 4).[21,43] The binary precursor method involves dispersing the A-cation ($A = Cs^+$, FA^+ or MA^+) and PbX_2 separately with the help of long chain ligands, such as oleic acid (OA) and oleylamine (OAm), in a high boiling point non-polar solvent, namely octadecene. The A-cation precursor is then swiftly injected into the PbX_2 precursor at elevated temperatures. As the PbX_2 is dispersed in the form of clusters, the A-cations intercalate into the PbX_2 clusters to form the $APbX_3$ lattice. On the other hand, in the ternary precursor method, the A-cation and Pb-precursor are dispersed in one mixture without the halide component, and the halide source is introduced separately. A variety of halide chemicals can be used as the precursor, including oleylammonium iodide, *tert*-butyl iodide, and trimethylsilyl iodide.[44–46] The precursors are dispersed as monomers and undergo a nucleation and growth scheme to form nanocrystals. Owing to different growth mechanisms and precursor choices, the resulting PeQDs from these two methods vary in size and shape uniformities, ligand shell compositions, and defect densities. For example, when synthesizing $CsPbI_3$ QDs with the

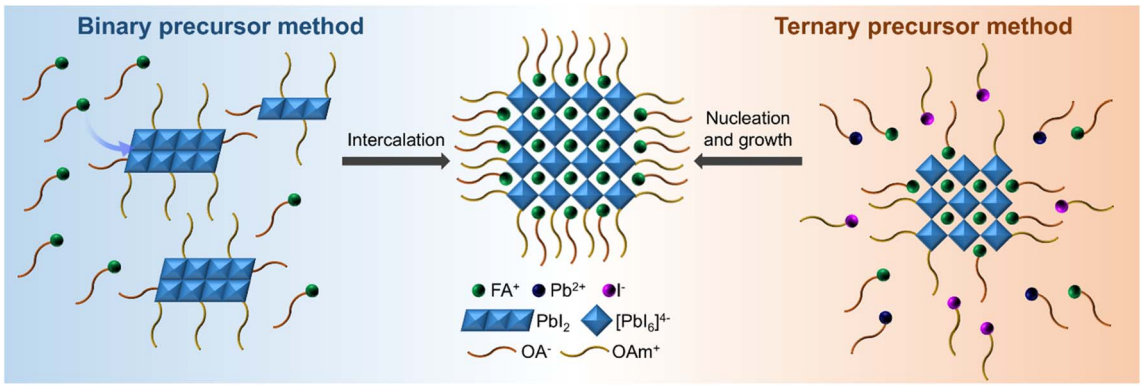

Fig. 4 Schematic illustration of the crystallization schemes of the binary precursor method and ternary precursor method for the synthesis of $FAPbI_3$ QDs.

binary precursor method, PbI_2 is in large excess.[18] The unreacted PbI_2 can affect cell performance by acting like insulating barriers or non-radiative recombination sites if not purified completely. When synthesizing $FAPbI_3$ QDs with the ternary precursor method, as oleylammonium iodide is in excess, the synthesized PeQDs will have a high density of OAm ligands on the surfaces.[47] Therefore, further engineering of the ligand exchange methods is needed to achieve high cell performance.

The precursor stoichiometry is critical in determining the quality of synthesized PeQDs by both methods. For example, in the binary precursor method of $CsPbI_3$ QDs, as the most studied composition of PeQDSCs, the Pb/Cs molar ratio is set to ~3 for controlled growth kinetics to achieve excellent optoelectronic properties and suppression of byproducts. However, halide/Pb is fixed when using the PbX_2 precursor as the only source for both the halide and Pb. One way to circumvent this restriction is to introduce additional halide sources in the precursor. Shi *et al.* introduced hydroiodic acid (HI) as an extra iodine source.[48] They detected plumbate ions with high order of iodide coordination in the HI-manipulated precursor, from PbI_3^- to PbI_4^- and PbI_5^-. They suggested that this change of precursors modified the nucleation number and the crystallization kinetics, producing high quality $CsPbI_3$ QDs and reducing lead-containing byproducts. HI-manipulated synthesis led to an increase in PeQD size from 10.25 to 11.84 nm and a significantly narrowed size distribution profile at the optimal HI concentration. The added HI filled surface iodine vacancies and produced near-unity PLQY. Benefiting from the improved size uniformity and defect passivation, the PCE of PeQDSCs improved from 14.07% to 15.72%. One of the important factors governing the synthesis is the reaction temperature, which determines the PeQD size and uniformity.[18] As the growth of PeQDs in hot injection is diffusion-limited, temperature controls the diffusion length of precursors in the reaction mixture, thus determining how large the "diffusion shell" around each nucleation site is. Therefore, a larger "diffusion shell" at higher temperatures allows more precursors to grow into one dot, leading to larger PeQD sizes. Since the hot injection synthesis of PeQDs follows the La Mer model,[49] an ice bath is usually required to quench the reaction once it reaches the Ostwald ripening region. Dong *et al.* proposed a precisely controlled PeQD synthesis strategy by reacting at a high halide : Pb molar ratio with ZnX_2 as an additional halide source in the precursor.[50] *In situ* PL measurements revealed that an equilibrium of halides established between the liquid medium and the PeQD lattices, altering the size dependency from kinetic control to thermodynamic control. As-synthesized $CsPbBr_3$ QDs decreased in size and improved in size uniformity at a higher Br : Pb molar ratio. High size uniformity plays an important role in achieving compact and ordered stacking of PeQDs in the solid-state film, which enhances the long-range electronic coupling and charge transport across the film. Zhang *et al.* introduced ZnI_2 as an additive in the precursor to synthesize $CsPbI_3$ QDs.[51] ZnI_2 reduces iodine vacancies and prevents iodine loss during the purification and ligand exchange processes by creating iodine-rich surfaces on $CsPbI_3$ QDs. The Zn-doped $CsPbI_3$ lattice also shows improved stability. By adding 10 mol% of ZnI_2, the PCE of the PeQDSCs improved from 13.98% to 16.07%, with a short-circuit current density, a J_{SC} of 17.25 mA cm^{-2}, a V_{OC} of 1.22 V, and a fill factor, FF, of 73.5%.

The ternary precursor method allows independent control of the precursor stoichiometry of all three elements. Specifically, the A/Pb precursors are solubilized using oleate in octadecene, and the halide precursor is then injected into the mixture to finish the reaction. Imran *et al.* proposed to use benzoyl halides as the halide precursor, which react strongly with nucleophilic ligands to release halide ions and trigger the nucleation and growth of PeQDs.[52] They managed to synthesize PeQDs with the $APbX_3$ ($A = Cs^+$, MA^+, FA^+ and $X = Cl^-$, Br^-, I^-) formula. The PeQDs tended to form lead halide terminated surfaces with A-sites passivated by OAm^+ ligands and subsequently showed high phase stability, narrow size distribution and high PLQY. Qian *et al.* explored the effect of precursor stoichiometry on $CsPbI_3$ QD synthesis.[53] They found that a byproduct Cs_4PbI_6 forms when using Cs : Pb : I = 1 : 1 : 3, while increasing the iodine ratio to Cs : Pb : I = 1 : 1 : 6 results in phase-pure $CsPbI_3$ QD products. At a ratio of Cs : Pb = 1 : 2, they were able to achieve phase-pure $CsPbI_3$ QDs with decent yield when varying Pb : I from 1 : 2 to 1 : 5 (*i.e.*, Cs : Pb : I = 1 : 2 : 4 to 1 : 2 : 10). Further increasing the iodine input ratio increases both the PL

lifetime and PLQY. With more OAmI added in the precursor, the surface iodine vacancies are effectively filled by I^- and Cs^+ are replaced by OAm^+ to form a stiff passivating ligand shell.[52,54,55] Moreover, the high halide ratio and OAm-rich surface ligand composition also contribute to the long-term stability of these PeQDs.[45]

3.2. Purification of PeQDs

The purification of synthesized PeQDs is a critical step in PeQDSC fabrication as it removes unreacted precursors and narrows PeQD size distribution. The purified PeQDs will then be concentrated to prepare dense PeQD inks that can be used for spin coating. After hot injection synthesis, the crude PeQD products contain unreacted precursors, byproducts and large sized MHP clusters. The purification step is usually conducted by centrifuging the PeQD colloid with the assistance of anti-solvents and redispersing the precipitate. The unwanted components will be decanted as they remain in the liquid phase. Due to the equilibrium of ligands between PeQD surfaces and the solvent medium, native ligands can detach from PeQD surfaces during the purification.[56] The loss of ligands often leads to surface defect formation or even decomposition of PeQDs. Therefore, careful design of the purification of PeQDs is necessary to prevent the formation of defects, especially iodine vacancies.

To restore the iodine vacancies formed on PeQD surfaces during purification, Jia *et al.* proposed a surface matrix curing strategy.[57] As PeQDs disperse in non-polar solvent, the ionic iodine source cannot dissolve and effectively react with PeQDs. They employed the nucleophilic substitution reaction between *tert*-butyl iodide and trioctylphosphine (TOP) to release iodide in non-polar solvent. The released iodides then fill the surface iodine vacancies, evidenced by the notable increase in the I/Pb ratio calculated from XPS results. The treated PeQDs exhibited improved PLQY and extended PL lifetime due to the reduction of surface defects and nonradiative recombination loss. These effects contributed to an improvement of cell PCE from 13.20% for pristine PeQDs to 16.21% after surface matrix curing. Li *et al.* incorporated methylammonium iodide (MAI) during the purification step of $FAPbI_3$ QDs.[58] DFT calculations showed that FA^+ and I^- vacancies with low formation energies would introduce shallow hole and electron trap states, respectively. The highly mobile MA^+ and I^- ions could effectively passivate these shallow trap states. They found that MAI also replaced native long-chain ligands by occupying their binding sites, and high MAI concentrations led to PeQD agglomeration due to excess removal of long-chain ligands. Notably, this purification promoted more homogeneous surface morphology of the $FAPbI_3$ QD film. Consequently, the champion cell exhibited a PCE of 15.10%, a J_{SC} of 17.30 mA cm^{-2}, a V_{OC} of 1.140 V, and a FF of 0.76.

The PeQD ligand shell contains both negatively charged OA^- and positively charged OAm^+ ligands. Spontaneous proton transfer can happen between OA^- and OAm^+ and cause them to dissociate from PeQD surfaces.[59] While both ligands play an important role in the synthesis and cannot be replaced, a ligand exchange during the purification can circumvent this unfavorable reaction. Zhang *et al.* proposed a liquid-phase ligand exchange using phenylethylamine (PEA) and 4-fluorophenethylamine (4FPEA).[60] After separating PeQDs from the crude product, they added PEA and 4FPEA to the PeQD colloid. They observed a PeQD size increase from 10.5 nm to 11.5 nm and a redshifted optical bandgap of PeQDs. Recent reports have shown that short-chain aromatic ligands could enhance charge carrier delocalization in PeQD solids.[61,62] The redshift was likely to stem from a mixed effect of reduced quantum confinement and enhanced charge delocalization. The liquid-phase ligand exchange provided sufficient passivation on PeQDs, manifesting in a prolonged charge carrier lifetime and increased PLQY. Furthermore, when the native long-chain ligands are replaced by short conductive ligands, the interfacial distances between adjacent PeQDs are reduced. This will promote stronger dot-to-dot interactions and shift the stacking mode of PeQDs to more compact and ordered (Fig. 5a). Additionally, the electronic coupling between PeQDs is also enhanced by the reduction of charge hopping barriers, leading to improved cell performance. Huang *et al.* introduced a liquid phase ligand exchange strategy using a bidentate ligand 2,5-thiophenedicarboxylic acid (DTA) in the second purification step of $CsPbI_3$ QDs.[63] Without purification, the PeQD assembled randomly after spin coating and formed solid-state films with uneven morphology and cracks. The DTA ligand anchored strongly onto surface iodine species and uncoordinated Pb^{2+}. After this treatment, the multidentate bonding capability of the DTA ligand enhances QD-to-QD interactions and promotes the formation of an ordered PeQD assembly, manifested by the sporadic Bragg spots in the 2D grazing-incidence wide angle X-ray scattering (GIWAXS) pattern (Fig. 5b). The structural uniformity smooths out the energy disorder, improving cell PCE from 14.08% to 16.14%, with a J_{SC} of 16.83 mA cm^{-2}, a V_{OC} of 1.262 V, and a FF of 0.76.

While the synthetic method determines the compositions of both the core and ligand shell of PeQDs, the purification method also needs to be designed accordingly to prepare PeQDs for desired applications. Chen *et al.* revealed that when using trimethylsilyl iodide (TMSI) as the halide source for the ternary precursor method, unreacted TMSI can anchor to the synthesized PeQD surfaces, interfering with the packing of PeQDs.[46] They proposed a chemical stripping treatment that utilizes nucleophilic TOP to strip off the byproducts on PeQD surfaces. The treated PeQDs show narrowed size distribution and tend to adopt long range stacking order when spin cast into solid-state films. This method also enhances the optoelectronic properties of PeQDs by reducing surface defects. The treated PeQDs exhibit an improved PCE from 14.28% under the control conditions to a champion PCE of 16.25%, a J_{SC} of 17.73 mA cm^{-2}, a V_{OC} of 1.23 V, and a FF of 74.5%.

3.3. Composition engineering

The MHP composition of PeQD cores plays a pivotal role in determining key optoelectronic properties, including the bandgap, Fermi level, and exciton binding energy, as well as structural properties such as phase stability and vacancy

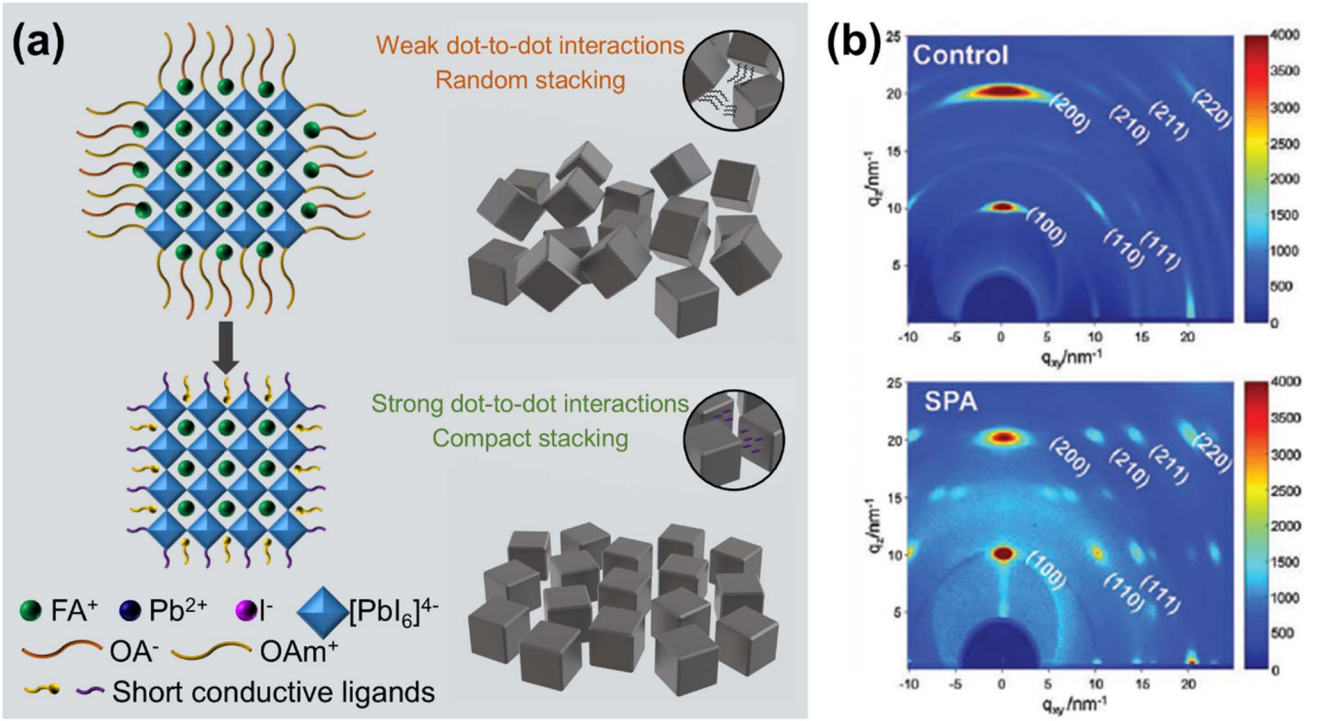

Fig. 5 Post-synthesis purification leads to ordered packing of PeQDs. (a) Schematic illustration of the *in situ* ligand exchange process, where short conductive ligands replace native long-chain ligands. The change in surface composition leads to stronger dot-to-dot interactions and promotes compact stacking of PeQDs. (b) Grazing incidence wide-angle X-ray scattering (GIWAXS) patterns of the control and SPA treated $CsPbI_3$ PQD films. Reproduced with permission from ref. 63. Copyright 2023 under license to John Wiley and Sons.

formation energy. As such, control over the MHP composition is imperative for the rational design and synthesis of high-performance PeQDSCs. While many studies focus on $CsPbI_3$ QDs, the transition to a mixed-cation composition of $FA_{1-X}Cs_XPbI_3$ can further improve the cell performance by adjusting the band alignment, improving charge carrier lifetime, and enhancing phase stability.[64] Stacking PeQDs with different band structures in the active layer can create a favorable band alignment across the cell to enhance the charge transfer and extraction.[41,42,65] In addition, bulk polycrystalline $FA_{1-X}Cs_XPbI_3$ films tend to have Cs segregation during crystallization and Cs migration under light illumination. Both issues can be greatly alleviated with nanocrystalline $FA_{1-X}Cs_XPbI_3$.

In 2017, Protesescu *et al.* first reported a hot injection synthesis method of $FAPbI_3$ QDs.[44] Unlike the synthesis of $CsPbI_3$ QDs where PbI_2 is in excess, $FAPbI_3$ QDs formed exclusively when FA^+ was in excess. $FAPbI_3$ QDs formed at lower reaction temperatures at around 80 °C due to their lower formation energy. In addition, a high OA concentration was needed for FA^+ to remain protonated in the reaction mixture. Violation of these reaction conditions would cause $FAPbI_3$ QDs to decompose. In light of these mismatches in reaction conditions, it is impractical to synthesize $FA_{1-X}Cs_XPbI_3$ with a mixed precursor of Cs^+ and FA^+. Instead, Hazarika *et al.* suggested a cation exchange method by intermixing $CsPbI_3$ and $FAPbI_3$ QDs.[35] $CsPbI_3$ and $FAPbI_3$ QDs were synthesized separately using the hot injection method and then mixed at room temperature for Cs^+ and FA^+ cations to diffuse spontaneously mediated by the liquid medium. This method could achieve a continuous tuning of the bandgap between $CsPbI_3$ and $FAPbI_3$ QDs by adjusting the ratio of each PeQD colloid. As shown in Fig. 6a, when two types of PeQDs are mixed, the cations can travel between PeQDs using oleate ligands as the 'shuttle' to provide mobility in non-polar solvent. The photoluminescence emission spectra will first show two separate peaks, which then merge into one to represent the final composition of $FA_{1-X}Cs_XPbI_3$.

The cation exchange process is largely governed by the chemical composition of the two PeQD colloids. Hao *et al.* reported a ligand-assisted cation exchange method for synthesizing high quality $FA_{1-X}Cs_XPbI_3$ QDs.[66] They pointed out that during the two centrifuge and redispersion cycles, the ligand density on PeQD surfaces reduces gradually, leading to "OA-rich" PeQDs after one cycle and "OA-less" PeQDs after two cycles. When they mixed the $CsPbI_3$ and $FAPbI_3$ QD colloids under "OA-rich" conditions, the PL spectra of the mixture initially exhibited two separate peaks from both $CsPbI_3$ and $FAPbI_3$ QDs, but then quickly merged into one peak with a wavelength between these two peaks, representing an $FA_{1-X}Cs_XPbI_3$ composition. The "OA-rich" PeQDs underwent a fast cation exchange process, owing to the increased diffusivity of cations with the assistance of ligands. Since the cations had low solubility in non-polar solvents, OA ligands chelated to the cations and offered high diffusivity for cations to travel between PeQD interfaces, facilitating the cation exchange reaction. The resulting PeQDs also exhibited lower defect densities, leading to

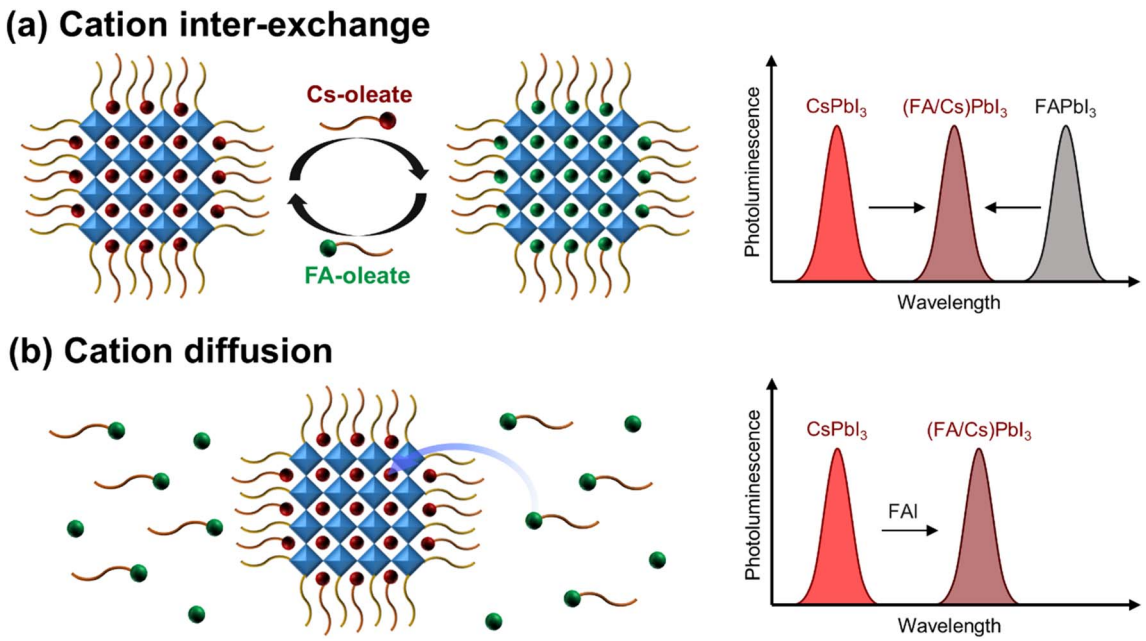

Fig. 6 Synthesis of mixed-cation $FA_{1-X}Cs_XPbI_3$ QDs. (a) The ligand-assisted cation inter-exchange reaction, where OA ligands act as molecular 'shuttles' to facilitate the inter-exchange of Cs^+ and FA^+ cations between $CsPbI_3$ and $FAPbI_3$ QDs. Initially separated PL peaks for $CsPbI_3$ and $FAPbI_3$ QDs merge into one peak representing the final $FA_{1-X}Cs_XPbI_3$ composition. (b) The antisolvent-assisted cation diffusion reaction. The antisolvent mobilizes the PeQD surfaces to allow the diffusion of FA^+ into the $CsPbI_3$ lattice. The single PL peak from initial $CsPbI_3$ QDs gradually shifts to one representing the final $FA_{1-X}Cs_XPbI_3$ composition. However, this method cannot fully replace Cs^+ to form $FAPbI_3$ QDs.

a high cell performance with a J_{SC} of 18.3 mA cm^{-2}, a V_{OC} of 1.17 V, a FF of 78.3% and a PCE of 16.6%. The processing solvent and PeQD concentration also greatly affect this cation-exchange reaction. Zhao *et al.* suggested that substituting the processing solvent from octane to toluene or chloroform largely accelerates this reaction.[67] With a high PeQD concentration of 70 mg ml^{-1} and a 1 : 1 ratio between $CsPbI_3$ and $FAPbI_3$ QDs, they obtained a fast cation exchange reaction that finishes within ~20 min. Zhao *et al.* further explored this cation exchange reaction with $MAPbI_3$ QDs.[68] The cation exchange between $FAPbI_3$ and $MAPbI_3$ QDs, two organic inorganic hybrid perovskite (OIHP) compositions, is much faster than that between the all-inorganic $CsPbI_3$ and OIHP QDs. The activation energy of the MA^+–FA^+ exchange reaction is ~0.35 eV, significantly lower than ~0.63 and ~0.57 eV for the exchange of Cs^+–FA^+ and Cs^+–MA^+, respectively. The $MA_{0.5}FA_{0.5}PbI_3$ QDs also exhibited the best cell performance among the mixed-cation PeQDs, with a PCE of 15.05%, a J_{SC} of 16.42 mA cm^{-2}, a V_{OC} of 1.19 V, and a FF of 77.02%, surpassing the PCE of 13.82% for $Cs_{0.5}MA_{0.5}PbI_3$ QDs and 14.20% for $Cs_{0.5}FA_{0.5}PbI_3$ QDs.

Due to the high hot injection synthesis temperature of $CsPbI_3$ QDs over $FAPbI_3$ QDs, the synthesized $CsPbI_3$ QDs usually have better size uniformity and less surface defect density. Obtaining $FA_{1-X}Cs_XPbI_3$ QDs by intermixing separately synthesized $CsPbI_3$ and $FAPbI_3$ QDs subsequently causes the transfer of low size uniformity from $FAPbI_3$ QDs into the final product. Therefore, directly doping $CsPbI_3$ QDs with FA^+ cations can lead to higher quality $FA_{1-X}Cs_XPbI_3$ QDs. As illustrated in Fig. 6b, with the help of antisolvent to mobilize $CsPbI_3$ QD surfaces, FA^+ can diffuse into the $CsPbI_3$ lattice to form $FA_{1-X}Cs_XPbI_3$ QDs. The photoluminescence emission spectra will show a gradual transition of composition from original $CsPbI_3$ to $FA_{1-X}Cs_XPbI_3$. However, this method cannot fully replace Cs^+ with FA^+ to form $FAPbI_3$ QDs and also cannot form $FA_{1-X}Cs_XPbI_3$ by diffusing Cs^+ into $FAPbI_3$ QDs since the solubility of Cs^+ is quite low. Jia *et al.* demonstrated an antisolvent assisted cation exchange method.[69] An FAI-containing antisolvent was used in the second purification step of synthesized $CsPbI_3$ QDs, where the FA^+ cation spontaneously diffuses into $CsPbI_3$ QDs. An azeotropic mixture of toluene and acetonitrile was used to both match the polarity of commonly used antisolvent methyl acetate and offer enough solubility for FAI. They were able to continuously tune the FA^+ ratio in $FA_{1-X}Cs_XPbI_3$ QDs from 0 to 0.57. The PL peak of $CsPbI_3$ QDs extended from 686 to 740 nm by increasing the FA^+ ratio, which was equivalent to an optical bandgap ranging from 1.81 to 1.68 eV. As a result, the cell performance was greatly improved from a PCE of 15.38% for the $CsPbI_3$ QDs with a J_{SC} of 17.55 mA cm^{-2}, a V_{OC} of 1.25 V and a FF of 70.1% to a champion PCE of 17.29% for the $Cs_{0.64}FA_{0.36}PbI_3$ QDs with a J_{SC} of 18.99 mA cm^{-2}, a V_{OC} of 1.23 V and a FF of 74.0%. Wang *et al.* further upgraded this method by introducing formamidinium tetrafluoroborate ($FABF_4$) into the antisolvent.[70] Since the antisolvent creates cation exchange channels by destabilizing the PeQD surfaces, surface defects inevitably form and act as nonradiative recombination sites. $FABF_4$ can effectively passivate these defects and create a compact surface matrix on PeQD surfaces. The $FABF_4$-PeQDs exhibit a high PLQY and a long PL lifetime, leading to a high PCE of 17.49% with a J_{SC} of 19.35 mA cm^{-2}, a V_{OC} of 1.22 V, and a FF of 74.12%.

Shi *et al.* explored the use of ytterbium as a B-site dopant for $CsPbI_3$ QDs.[71] They solubilized $YbOAc_3$ along with PbI_2 as a precursor in the binary precursor synthesis. Yb^{3+} entered the PeQD lattice and occupied the Pb^{2+} site, causing the PeQD lattice to shrink due to the small size of Yb^{3+}. They found that the Yb-doping did not alter the optical bandgap of PeQDs, only yielding PeQDs with lower defect density. A champion PCE of 13.12% was achieved with 20% Yb-doping. The Yb-doping also benefits long-term cell stabilities as the doped PeQDs exhibited enhanced resistance to heat and moisture.

4. Surface modification of solid-state PeQD films

The optoelectronic properties of solid-state PeQD films are highly dependent on surface ligands, which significantly impact both surface states and QD–QD interactions. When PeQDs are assembled into thin films, their electronic structure and charge carrier dynamics become particularly sensitive to variations in surface composition. For example, the dissociation of native ligands can result in surface vacancies that function as trap states, whereas incomplete ligand exchange may introduce dielectric barriers that impede efficient charge transport. Consequently, precise chemical control over PeQD surface composition is crucial for enhancing the performance of PeQDSCs.

4.1. Layer-by-layer ligand exchange

Due to the insulating nature of the native long-chain ligands on PeQD surfaces, the spin coated PeQD film is almost nonconductive in its pristine state. Luther and coworkers introduced a layer-by-layer ligand exchange method to construct conductive solid-state PeQD films to be used as the photoactive layer of PeQDSCs.[18] They dipped a spin coated PeQD film into antisolvent for the native ligands to dissociate. The PeQDs then electronically connected spontaneously. Owing to the limited concentration of PeQD ink, one spin coating cycle usually results in a 70–100 nm thick film, which is not sufficient for solar cells. As a common practice, PeQDSCs require 3–5 spin coating cycles to construct a solid-state PeQD film with a thickness of 200–500 nm. This dipping process helps solidify the PeQD film so that the following spin coating cycles will not redissolve the previous PeQD film.

The soft and thick ligand shell leads to PeQDs with a less cubic shape than their cores when stacking into a film.[72] Considering the short residence time and non-perfect size distribution, the PeQDs usually stack randomly to form a mesoporous film in a pristine PeQD film obtained *via* spin coating. The mesopores provide channels for the ligand exchange solution to penetrate and for dissociated ligands to leave the film during the dipping step. When the ligand exchange process strips off the thick ligand shell, the PeQD film structure collapses towards the substrate, causing a volume shrinkage and forming a compactly stacked film.[73] During this process, short-chain ligands replace native long-chain ligands to bring adjacent PeQD surfaces into intimate contact or even induce oriented attachment.[74] An ordered packing mode with aligned in-plane orientation is highly desired at this stage as it establishes fast vertical charge transport channels between two electrodes. The steric effect of exchanged surface ligands can be rationally designed to achieve long-range ordered packing, which enhances electronic coupling and charge transport across the solid-state PeQD film.[75] Besides, a narrow size distribution will suppress structural defects, such as voids.

The processing solvent and environment are of great importance to the ligand exchange process. As conventional ligand exchange methods mainly use methyl acetate (MeOAc) as the processing solvent, it was found that the humidity of the processing environment imposes significant influence on the cell performance. Wheeler *et al.* revealed the working mechanism of MeOAc during ligand exchange in a humid environment.[76] They suggested that MeOAc undergoes hydrolysis and produces acetic acid, which targets to replace the negatively charged oleate ligands (Fig. 7a). They aimed to fabricate $CsPbI_3$ QDSCs under controlled humidity. At RH < 3%, they only achieved uneven coverage of PeQD films. This indicates that due to the weak ligand exchange strength without the help of moisture, the PeQDs retain their long-chain ligand shell and redissolve when a successive layer is coated. At RH > 30%, the PeQD film turned yellow as a sign of δ-phase $CsPbI_3$ formation. As a result, they obtained optimal cell performance at 19–24% RH. It is worth noting that they could not achieve comparable cell performance when they tried to replicate this method by adding water to dry MeOAc and fabricate PeQDSCs in a dry environment. This highlights that it was the moisture adsorbed at PeQD surfaces that assisted the proposed ligand exchange mechanism rather than the hydrolysis product of MeOAc under a humid environment.

The current antisolvent based ligand exchange method requires delicate control of the ligand density on PeQD surfaces. High ligand density impedes charge transport and may cause PeQD films to redissolve, while low ligand density creates surface defects and may even cause PeQDs to decompose. We note that the ligand shell composition of PeQDs can vary according to different synthesis methods. Ding *et al.* reported that the ligand composition in the precursor determined the surface ligands of $FAPbI_3$ QDs.[47] With the binary precursor method, as both OA and OAm were used to solubilize the PbX_2 precursor, they are both present on PeQD surfaces as the major composition. Proton exchange between OA^- and OAm^+ ligands would destabilize PeQDs and form halide vacancies. The humidity assisted ligand exchange using MeOAc was therefore effective on ligand exchange of these PeQDs. On the other hand, the ternary precursor method used excess amounts of OAmI as the precursor, which then consisted of the major composition of the ligand shell in PeQD products. The protonated OAm^+ suppressed the proton exchange reaction and led to less defect density, but the ligand exchange strength should be enhanced by adding alkylamine or alkylammonium to target OAm^+ ligands.

During the ligand exchange process, the polar antisolvent mobilizes PeQD surfaces and allows exchange of species to happen. While the main purpose of this process is to replace

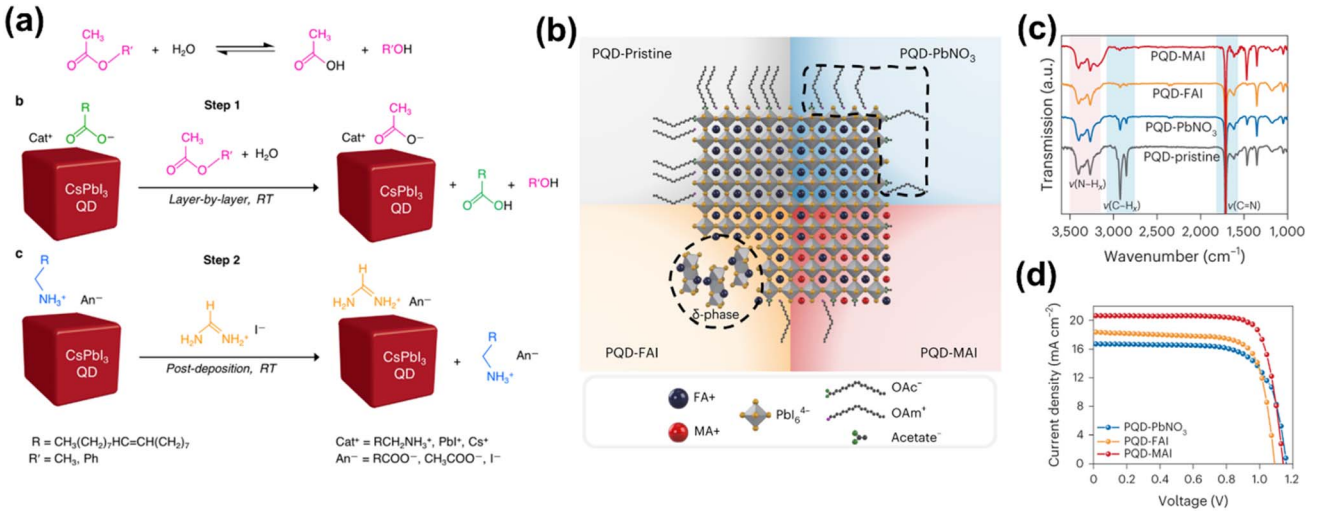

Fig. 7 Layer-by-layer ligand exchange. (a) Mechanistic schemes of humidity assisted ligand exchange. Reproduced with permission from ref. 76. Copyright 2018 American Chemical Society. (b) Schematic illustration of crystal and surface bonding states of pristine PeQDs, after conventional ligand exchange (with $Pb(NO_3)_2$) and FAI/MAI assisted ligand exchange. (c) FTIR spectra of PeQD films before and after ligand exchange. (d) *J*–*V* characteristics of PeQD solar cells. Reproduced with permission from ref. 20. Copyright 2024 under exclusive license to Springer Nature Limited.

native long-chain ligands with short-chain conductive ligands, it sometimes leads to the formation of defects such as vacancies and decomposed lattices. Therefore, preserving the structural integrity is important in maintaining the optoelectronic performance of synthesized PeQDs. Shivarudraiah *et al.* added FAI in ethyl acetate (EtOAc) for layer-by-layer ligand exchange.[77] While humidity assisted release of OAc^- could target to replace OA^- ligands, FTIR suggested that there was still a portion of long-chain ligands in the PeQD film, which was ascribed to OAm^+ ligands. The added FAI dissociated into FA^+ and I^- ions. The FA^+ replaced OAm^+ ligands, while the I^- suppressed the formation of iodine vacancies. Multiple iodide-based salts, such as guanidinium iodide (GAI), phenethylammonium iodide (PEAI), and choline iodide (CI),[73,78] were also used to achieve efficient surface passivation and bridging between PeQDs. Moreover, pseudohalides were used for stronger passivation of uncoordinated Pb^{2+} sites. Zhang *et al.* replaced FAI with formamidine thiocyanate (FASCN) for the ligand exchange process.[79] FASCN first dissociates into FA^+ and SCN^- ions and then provides combined effects of facilitating the removal of long-chain ligands and filling the surface vacancies. SCN^- formed strong Pb–S bonds and density functional theory (DFT) calculations showed that it removed the unfavorable trap states formed by iodine vacancies.

When the antisolvent mobilizes PeQD surfaces, the salt additive can penetrate into PeQD films and alter their composition. Aqoma *et al.* improved this method by using an isopropyl alcohol (IPA) solution of alkylammonium iodide as the ligand exchange solution for $FAPbI_3$ QDSCs.[20] They used $FAPbI_3$ QDs to build the active layer, which have a narrower bandgap than $CsPbI_3$ QDs and hence higher theoretical cell efficiency as a single-junction according to the Shockley–Queisser limit.[80] IPA has a higher polarity than conventionally used MeOAc to accelerate the dissociation of native long-chain ligands. The crystal structure and surface bonding schemes of PeQDs before and after this ligand exchange are demonstrated in Fig. 7b. When adding FAI into the ligand exchange solution, they found that an undesired δ-phase formed in the $FAPbI_3$ QD film after ligand exchange, which deteriorated the V_{OC}. The dissociation of OAm^+ altered the PeQD surface strain and caused a phase transition of $FAPbI_3$ from an α-phase to a δ-phase. They solved the unwanted phase transition by incorporating methylammonium iodide (MAI) into the ligand exchange solution. As MA^+ diffuses into the $FAPbI_3$ lattice, it releases the microstrain by reducing the cubo-octahedral volume and stabilizes the α-phase thermodynamically.[81] FTIR spectra showed that MAI could further drive the replacement of long-chain ligands to completion, greatly enhancing the conductivity of the PeQD film (Fig. 7c). Additionally, the MA^+ and I^- ions suppress surface defect formation by filling the A-/X-site vacancies left by the dissociated ligands. The high mobility of MA^+ ions in the MHP lattice[68] and low formation energy of MA-incorporating MHP suppressed the formation of byproducts during this soaking step. With this method, as shown in Fig. 7d, they achieved a record certified PCE of 18.06%, with a J_{SC} of 20.89 mA cm^{-2}, a V_{OC} of 1.14 V, and a FF of 0.76.

While adding ionic salt is an effective method to suppress defect formation, neutral reagents can form stronger bonding to PeQD surfaces and therefore induce enhanced passivation effects. For example, amino acids, including glycine, alanine, and lysine, can generate both carboxyl and ammonium functional groups due to their zwitterionic nature, which interact strongly with Pb^{2+} and I^- sites, respectively.[82,83] DFT calculations show that the binding energy of the carboxyl of glycine to the PeQD surface, $E_{binding}$, is 4.558 eV, which is higher than $E_{binding}$ = 4.441 eV of the carboxyl of OA^- to the PeQD surface. However, the ammonium of glycine bonds weaker than OAm^+ ligands, with an $E_{binding}$ of 4.156 eV and 4.285 eV, respectively.

Amines react irreversibly with OA^- ligands *via* the acylation reaction, allowing a controlled ligand exchange scheme under dry conditions.[84] Ding *et al.* employed glycocyamine (GLA) due to its strong bonding with the PeQD lattice by multiple ionic interactions and coordination interactions.[85] The guanidinium and carboxyl terminal groups form hydrogen bonding with I^- and coordination bonding with Pb^{2+}, respectively. Ultraviolet photoelectron spectroscopy (UPS) measurements indicated that the GLA treatment downshifted the Fermi level of PeQDs by 0.38 eV compared to traditional ligand exchange with $Pb(NO_3)_2$, promoting a better band alignment between the CBM of PeQD and electron transport layer (ETL). Moreover, they were able to finely tune the junction band structure by applying different ligand exchange solutions on different layers of PeQD stacks, and the champion device delivered a PCE of 15.34%, with a J_{SC} of 18.03 mA cm^{-2}, a V_{OC} of 1.16 V, and a FF of 0.73. Secondary amines with electron donating groups to enhance alkalinity lead to a more reactive ligand removal scheme. We note that the amine group can react with FA^+ to form bulky amidinium ligands,[86] potentially changing the ligand exchange reaction stoichiometry. Overall, rational design of the ligand exchange solution composition and the processing environment according to the PeQD core and ligand shell composition are critical in achieving high performance PeQDSCs.

4.2. Post-deposition soaking

Sanehira *et al.* proposed a post-deposition soaking method to enhance the charge mobility of $CsPbI_3$ PeQD films (Fig. 8a).[19] Specifically, they first deposited PeQD films following layer-by-layer spin coating and ligand exchange cycles. After stacking a thick PeQD film, they soaked the film in an ethyl acetate (EtOAc) solution with AX ($A = MA^+$, FA^+, Cs^+ and $X = I^-$, Br^-) for 10 s to electronically couple the PeQDs. As shown in Fig. 8b and c, time-of-flight secondary ion mass spectrometry (ToF-SIMS) indicated that FA^+ diffused into the PeQD film and concentrated at the surface periphery of the film. Fig. 8d demonstrates the time-resolved terahertz spectroscopy (TRTS) data of representative PeQD films, MHP films, and traditional PbS and PbSe QD films. The post-treatment increased the charge carrier mobility of $CsPbI_3$ QD films from 0.23 to 0.50 $cm^2\ V^{-1}\ s^{-1}$, surpassing that of lead chalcogenide QD films. The target cell exhibited a certified PCE of 13.43%, with a J_{SC} of 15.246 mA cm^{-2}, a V_{OC} of 1.1626 V, and a FF of 76.63%. Due to the excellent improvement in electronic properties, this post-deposition soaking method has been widely adopted to improve the performance of PeQDSCs. This method removes long-chain ligands and forms a thin surface matrix on PeQDs to induce a compact packing of PeQDs.[87] The soaking process usually incorporates a salt additive in the solution, such as FAI, for two purposes: (1) to further replace the remaining positively charged long-chain ligands after the layer-by-layer deposition and (2) to compensate for the A-/X-site vacancies formed during ligand dissociation. These structural changes reduce the charge transport barrier and prevent nonradiative recombination at the interfaces between adjacent PeQDs.

When PeQD films are in contact with the soaking solution, the polar solvent mobilizes the ionic bonding on PeQD surfaces, promoting the exchange of surface species. The dielectric constant of a polar solvent then becomes a critical measure of the strength of the surface modifications, as it describes the electrostatic interactions between solvent molecules and the charged species on PeQD surfaces. Jia *et al.* systematically studied the effect of the solvent dielectric constant on the soaking process.[78] They screened a series of protic alcohols as pure solvent for the soaking step and found that 2-pentanol (2-PeOH) improved the cell PCE to 14.86% from 13.98% for EtOAc. FTIR and XPS results showed that 2-PeOH facilitated the dissociation of OAm ligands while retaining PeQD structures. DFT calculations confirmed that 2-PeOH formed strong hydrogen bonding with N–H bonds of OAm^+, while the interactions with EtOAc were too weak. Protic alcohols attack carboxyl ligands by protonation. The hydrogen bond donor (HBD) acidity describes the carboxyl dissolving capability. They pointed out that solvents with high HBD acidity could lead to PeQD phase transitions and degradation. They further introduced choline iodide (ClI) in the soaking solution and achieved a champion PCE of 16.53%, with a J_{SC} of 17.80 mA cm^{-2}, a V_{OC} of 1.27 V, and a FF of 0.731, owing to the enhanced conductivity and reduced defect density of PeQD films.

The conventional method of PeQDSC fabrication includes cycles of spin coating and ligand exchange for the layer-by-layer deposition of PeQDs and a post-deposition soaking step to enhance the electronic coupling of the solid-state PeQD films. We want to point out that the solutions used for these two steps are distinctly different, as the soaking step is sensitive to reaction duration. However, the solid-state PeQD films are subjected to the ligand exchange solution multiple times, making it impossible to control the reaction time for each PeQD layers. The ligand density on PeQDs, which determines the optoelectronic properties of the final PeQD film, is therefore in a dynamic state during the whole fabrication process. The ligand density drops when dipping the solid-state PeQD films into the ligand exchange solution. Each layer of PeQD depositions has different ligand densities as they are dipped multiple times depending on the sequence of spin coating. Therefore, the total thickness of the PeQD film, the concentration of PeQD ink, and the ligand exchange solution need to be synergistically designed. During the post-deposition soaking, the entire PeQD film is immersed in the soaking solution. As the PeQD film usually possesses a certain level of porosity, the soaking solution can penetrate deep into the film and modify the electronic structures. Therefore, the soaking reagent needs to be carefully designed. For example, Cs salts are often not so efficient in this method due to their poor solubility and the poor mobility of Cs^+ ions. FAI is a commonly used soaking reagent, while pseudohalides, such as thiocyanate (SCN^-), can also be used for effective passivation of X-sites.[87,88]

4.3. Conductive PeQD ink

The PeQD ligand shell composition OA/OAm was designed to optimize surface passivation, colloidal stability and PLQY. This

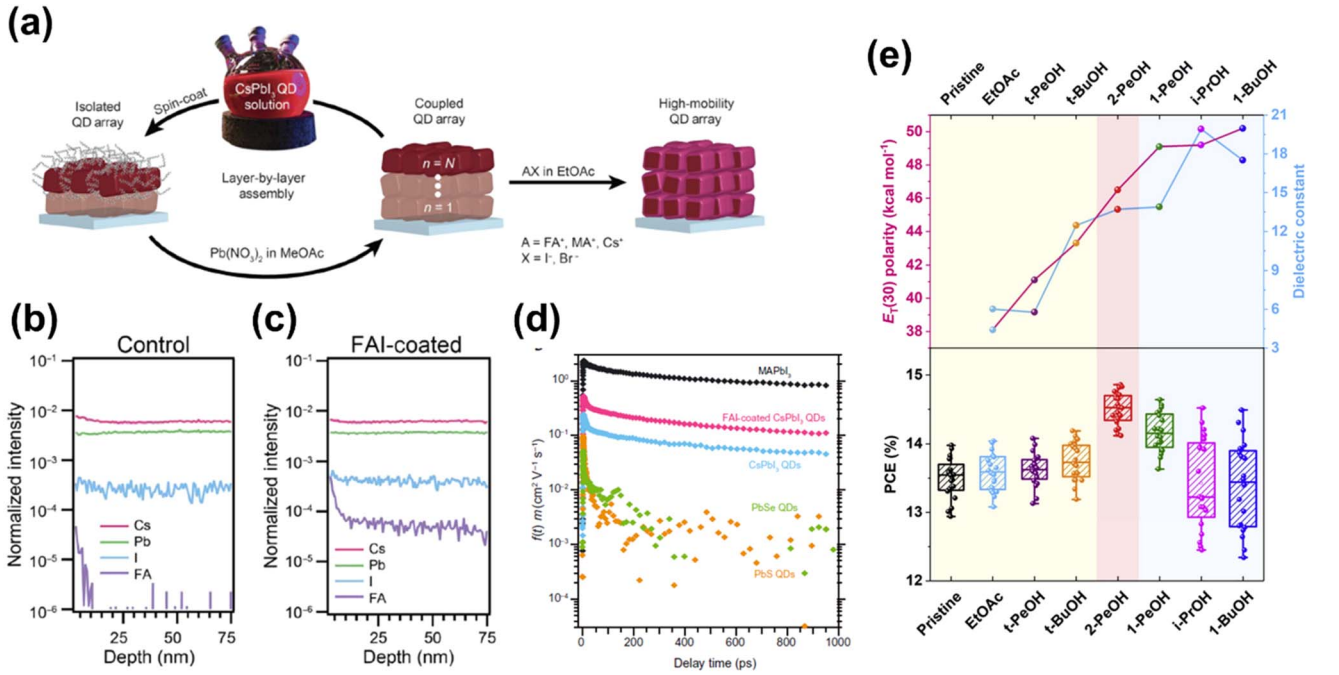

Fig. 8 Post-deposition soaking. (a) Schematic illustration of the film deposition process and post-deposition soaking. ToF-SIMS depth profile of $CsPbI_3$ QD films (b) without and (c) with an FAI soaking. (d) Time-resolved terahertz photoconductivity measurements of the charge carrier mobility in the films of the $CsPbI_3$ control sample (blue) compared to the FAI-coated $CsPbI_3$ QD films (pink) along with a traditional $MAPbI_3$ (black) thin film and films of 6 nm PbSe QDs (orange) and 3 nm PbS QDs (green). Reproduced with permission from ref. 19. Copyright 2017, American Association for the Advancement of Science. (e) $E_T(30)$ polarity and dielectric constant values of processing solvent for post-deposition soaking with the corresponding PeQDSC PCEs obtained with these solvents in a neat state. Reproduced with permission from ref. 78. Copyright 2022 under exclusive license to Elsevier.

composition is not ideal for photovoltaic applications due to its insulating nature, and therefore a ligand exchange step is required to enhance the conductivity of the PeQD film. However, this fabrication method sets the ligand density of the PeQD film into a dynamic state as the film is repetitively applied to antisolvent for layer stacking. The ligand density is tightly bound to many critical properties of PeQDs, including conductivity, defect density, and structural stability. The performance of PeQDSCs can often be out of control and irreproducible. A ligand shell with short-chain ligands can provide moderate conductivity to spin coated pristine PeQDs, so the ligand exchange step is no longer required. By circumventing the ligand exchange step, we can establish a structure–performance-relationship for PeQDSCs instead of relying on processing-specific results, even though short-chain ligand PeQD colloids might be in a meta-stable state due to the insufficient steric effect.

Zhang *et al.* proposed a sequential acylation-coordination protocol (SACP) to synthesize conductive colloidal PeQD inks.[16] The synthesized $FAPbI_3$ QDs first underwent an acylation reaction with di-*n*-propylamine (DPA) to break the acid–base equilibrium of the native ligand shell and facilitate the dissociation of native ligands. They then added a Lewis base molecule, triphenylphosphine (TPP), into the PeQD mixture as a restoration of the ligand shell and to passivate defects and improve dispersity. DFT calculations revealed the binding energy of TPP to the PeQD surface to be 3.23 eV, much stronger than the 1.10 eV of OA. The conventional PeQD film deposition method involves a layer-by-layer deposition and ligand exchange cycle. The PeQD films could easily form cracks due to volume shrinkage by ligand shell thickness reduction. For comparison, PeQD inks prepared by the SACP only needed one deposition step and produced thick PeQD films with improved morphology homogeneity. They found that the TPP passivation suppressed nonradiative recombination, reduced energetic disorder, and extended charge carrier lifetime. PeQDSCs fabricated with conductive PeQD ink exhibited an improved PCE of 16.61% from 14.64% for the control cell. Thanks to the processing simplicity, they successfully fabricated large-area PeQDSCs with blade-coating, demonstrating an optimal PCE of 16.02%.

4.4. Nanocomposites

One critical advantage of PeQDs in device fabrication is that their crystallization and deposition are decoupled. PeQDs are synthesized, purified, and then concentrated into a dense PeQD ink for device fabrication. This allows seamless integration with hole and electron transport materials, as transport materials are added into PeQD ink and would not interfere with the crystallization. Hu *et al.* incorporated phenyl-C61-butyric acid methyl ester (PCBM) with PeQDs to form a hybrid layer at the PeQD/ETL interface.[89] Specifically, they blended PCBM into PeQD ink and coated it on ETL substrates. They then spin coated

PeQD ink without PCBM to finish stacking the PeQD layer. The PCBM molecules form fast electron transport channels, and the carboxyl moieties bond to uncoordinated Pb^{2+} sites. The projected density of states (pDOS) from the DFT calculations showed that PCBM helped remove the trap states caused by Pb^{2+} vacancies by receiving electrons from the perovskite lattices. With this strategy, they demonstrated a PCE of 12.3% with a flexible device structure. The solubility of PeQDs in non-polar solvents enables their integration with many polymeric semiconductors. Ji *et al.* compared multiple conjugated polymers in forming bulk heterojunction (BHJ) layers with PeQDs.[90] Han *et al.* varied the PCBM concentration in $CsPbI_3$ QD ink and obtained a gradient of heterojunctions between these hybrid films.[91] They argued that PCBM anchored to PeQD surfaces and imposed surface dipoles, which gradually deepens the Fermi level and hence the CBM position. The pronounced PL quenching at high PCBM concentrations suggested that a type II heterojunction formed between PCBM and $CsPbI_3$ QDs, which favors charge separation at the interface. Thanks to the solvent compatibility, they were able to blend various conjugated polymers (PBDB-T, PTP8, PTB7-Th and PTB7) into PeQD ink to form BHJ layers at the PeQD/hole transport layer (HTL) interface. The BHJ films exhibited prominent PL quenching behaviors, suggesting charge separation at the PeQD/polymer interfaces. By optimizing the polymer/PeQD ratio, they achieved a desired morphology of the hybrid film without phase segregation. The polymers then contributed to eliminating film morphological defects, such as cracks and pinholes, which would otherwise become nonradiative recombination centers. With PBDB-T, due to its optimal highest-occupied molecular orbital (HOMO) level, they improved the PCEs of $CsPbI_3$ and $FAPbI_3$ QDSCs from 13.1% and 11.6% to 13.8% and 13.2%, respectively.

These BHJ films of transport materials and PeQDs can also be established during the ligand exchange process. Xue *et al.* introduced ITIC in the EtOAc ligand exchange solution for $FAPbI_3$ QDSCs.[92] During the ligand exchange, ITIC remained in the PeQD film to form a heterostructure. They observed similar PL quenching behaviors to the BHJ films mentioned above, highlighting the versatility and compatibility of PeQDs in forming heterostructures. Yuan *et al.* employed Y6-series molecules in the ligand exchange solution to form type II heterojunctions with $CsPbI_3$ QDs, with an aim to enhance charge transport and extraction.[93] *Ab initio* calculations showed that the Y6–F molecule resided at a shorter distance from $CsPbI_3$ QD surfaces than Y6–H and Y6–Cl, allowing for the best electronic coupling with PeQDs. The Y6–F hybrid cell exhibited an improved V_{OC} of 1.26 V, an improved J_{SC} of 15.81 mA cm^{-2}, and a champion PCE of 15.05%, surpassing those of the control cell and Y6–H and Y6–Cl hybrid cells. These enhancements were ascribed to the strong interactions between Cs–F and Pb–F, which promoted defect passivation, efficient charge separation, and smooth film morphology. In light of these findings, PeQDs are capable of constructing multiple heterojunctions ranging from molecule/PeQD interfaces to polymer/PeQD BHJs and hybrid film/transport layer planar junctions. Incorporating versatile device architectures and transport materials with proper energy alignment will further improve the cell performance of PeQDSCs.

5. Outlook

PeQDSCs have witnessed significant progress in recent years, benefiting from the unique properties of PeQDs, such as facile synthesis, high structural tunability, low pristine defect density, and versatile processability. Advances in synthesis and surface modification methods have contributed to improved device performance through more efficient charge transport and reduced non-radiative recombination losses. Despite these advancements, further efforts are required to enhance the synthesis and surface modification techniques and to address the remaining challenges in long-term stability, in order to fully realize the potential of PeQDSCs for scalable and efficient solar cells.

For the synthesis of PeQDs, it is crucial to develop methods that produce PeQDs with intact surfaces and narrow size distributions. The conventional hot-injection method remains the predominant approach, wherein PeQD size is determined by diffusion-limited crystallization kinetics occurring on a sub-second timescale. Consequently, this often leads to broad size distributions, necessitating post-synthetic purification steps such as centrifugation to narrow the size distributions. However, the size distribution critically impacts the packing behavior of PeQDs during film deposition. Monodisperse PeQDs tend to stack more compactly with their facets aligned, thereby reducing charge transport barriers and enhancing device performance.[94] Although kinetically and thermodynamically controlled synthetic strategies have demonstrated potential for producing highly monodisperse PeQDs,[50,95,96] these methods suffer from low yields and have not yet been adopted for practical device fabrication, highlighting a key challenge that remains to be addressed. Moreover, the scalability of the hot-injection method is limited due to its sensitivity to reaction volume, restricting its application for large-area solar cells. Microfluidic synthesis offers a promising alternative, providing enhanced control over reaction parameters, minimized batch-to-batch variability, and scalability suited for industrial implementation.[97,98] Looking ahead, while the legacy solvent octadecene provides a chemically and thermally stable reaction environment, it requires the use of long-chain insulating ligands such as oleate and oleylammonium to solubilize precursors. The resulting PeQDs are typically capped with an insulating ligand shell, necessitating ligand exchange processes that inevitably introduce surface vacancies, which can act as charge traps to degrade device performance. Future research should explore the use of polar solvents and short ligands to achieve either ionic colloidal stability or metastability.[99] Such approaches could eliminate the need for ligand exchange and enable the direct transfer of well-passivated surfaces from solution-phase synthesis to solid-state devices, ultimately improving the performance and scalability of PeQDSCs.

There remains substantial room for improvement in the surface modification of PeQDSCs. The development of novel short-chain ligands is particularly important. These ligands

should exhibit strong binding affinity to the PeQD surface while promoting facet-to-facet interactions, thereby facilitating oriented packing and enhancing electronic coupling between PeQDs. Additionally, ligands that impart higher colloidal stability are valuable for increasing the solubility limit of PeQDs in solutions. This improvement would allow for the deposition of thicker active layers with fewer coating cycles, consequently reducing the likelihood of defect formation during fabrication. Given that PeQDs typically form mesoporous films with considerable inter-particle voids, incorporating bridging materials to fill these gaps can significantly enhance charge transport. Such materials may include small-sized nanocrystals, multidentate flexible ligands,[100] conjugated polymers,[62,90,101] or other conductive fillers. Overall, further refinement of the chemical design of PeQD inks is critical to simplifying the fabrication process and ensuring the effective transfer of the intrinsic optoelectronic properties of PeQDs into solar cells. Furthermore, improvements in ink formulation and processing compatibility are essential for enabling the scalable production of large-area and flexible PeQDSCs.

PeQDs exhibit notable stability in colloidal form, maintaining high PLQY over extended periods due to their well-passivated surfaces. When processed into solid-state films, PeQDs also demonstrate considerable structural robustness. In contrast to bulk perovskite thin films, which often undergo phase transitions from photoactive black phases to photoinactive yellow phases under thermal or photo-induced stress, PeQDs are less susceptible to such degradation.[30,102,103] This enhanced phase stability arises from their nanoscale dimensions, which prevent the accumulation of microstrain. Any lattice distortions induced by changes in temperature or illumination can be effectively relaxed at the grain boundaries, mitigating stress buildup. However, despite their advantages, PeQDs exhibit vulnerability to humidity due to their large surface area and the increased number of diffusion pathways available for moisture ingress. Nevertheless, PeQDSCs benefit from the dielectric confinement effect, which imparts a high resistance to halide segregation. Given their intrinsic phase stability and resistance to compositional instability, PeQDSCs hold significant promise for long-term operational stability. Further investigations are needed to fully understand and harness these stability advantages under real-world conditions.

To further improve the stability of PeQDSCs, effective defect passivation and optimized device architecture are essential. A major degradation pathway originates from surface vacancies on PeQDs, which are prevalent due to their high surface-to-volume ratio. These defects serve as charge traps to cause non-radiative recombination losses and facilitate ion migration which leads to local stoichiometric imbalances. In severe cases, they can initiate undesirable phase transitions, such as the formation of non-photoactive yellow phases. Surface vacancies are often introduced during the layer-by-layer ligand exchange process, where the use of antisolvents mobilizes surface ligands, potentially causing their spontaneous detachment. Mitigating this issue requires ligand exchange additives that not only replace native ligands but also effectively passivate exposed coordination sites. Additionally, instability can arise from residual byproducts and the presence of non-uniformly sized PeQDs, particularly those at the extremes of the size distribution. Such PeQDs exhibit increased susceptibility to environmental degradation and lower activation energies for decomposition. Synthesis residues can participate in unwanted side reactions, exacerbating instability. Therefore, the development of high yield, monodisperse PeQD synthesis methods, coupled with efficient and clean purification techniques, remains a pressing need. Currently, most PeQDSCs employ the conventional n–i–p architecture and use doped Spiro-MeOTAD as the HTL, due to its appropriate energy alignment and high hole mobility. However, doped Spiro-MeOTAD contributes to performance degradation due to the hygroscopic nature of lithium-based dopants, mobility loss from dopant segregation, and iodine migration from the PeQD layer.[104,105] The exploration of dopant-free HTLs offers a promising route to mitigate these issues.[106,107] Additionally, adopting inverted p–i–n architectures with more stable transport layers could further enhance device durability. In particular, self-assembled monolayer (SAM) molecules offer dual functionality of both passivating the transparent conductive oxide (TCO) surface and facilitating improved charge extraction through favorable interfacial interactions with PeQDs.[108–110]

The inherent structural tunability of PeQDs enables their integration into a variety of solar cell architectures from single-junction to tandem solar cells, either all-perovskites or combined with other photoactive materials. For example, two-terminal tandem solar cells present a critical challenge in photocurrent matching because the bandgaps of both the top and bottom sub-cells must be synergistically designed to maximize photocurrent generation. Conventional wide-bandgap (WBG) MHP absorbers often suffer from light-induced halide segregation, compromising their long-term stability. In contrast, PeQDs offer a broad range of tunable bandgaps through modulation of A-site cations and halide compositions, while maintaining robust phase and compositional stability due to effective surface passivation and confinement. These characteristics position PeQDs as promising candidates for the top cell in two-terminal tandem architectures, with broad compatibility across various bottom cell technologies. Additionally, the nanocrystalline nature of PeQDs allows for efficient strain relaxation, enhancing their potential for use in flexible photovoltaic devices. Moreover, the decoupling of crystallization and film deposition in PeQDSC fabrication enables the adoption of scalable and versatile deposition techniques such as roll-to-roll printing, spray coating, and slot-die coating. Continued research and development are needed to fully realize the potential of PeQDs in large-area solar cell applications.

In this review, we discussed the unique properties of PeQDs, advanced strategies for their synthesis and surface modification, and recent advances in chemistry for PeQDSC fabrication. In particular, the compositions of both the PeQD core and the ligand shell are critical to achieving high performance PeQDSCs. These compositions, along with the chemical treatments used to tailor them, directly influence key properties such as the band structure, defect density, QD–QD electronic

coupling and film morphology that directly impact PeQDSC performance. Despite notable progress in PeQD synthesis and surface engineering, several challenges and opportunities remain. Scalable synthesis approaches that yield PeQDs with uniform size, structural integrity, effective surface passivation, and conductive ligands are essential for further improving PeQDSC performance. Expanding the library of conductive ligands can inform the development of more effective purification methods, while eliminating the ligand exchange step with conductive PeQD inks may significantly enhance both performance and reproducibility. Moreover, interface engineering, particularly at the buried interface of PeQD films with charge transport layers, offers a promising route to reduce interface defect density and facilitate more efficient charge extraction. Finally, the transition to an inverted device architecture may improve stability by avoiding the use of doped hole transport layers. With continued advances in scalable fabrication, compositional control, and interface optimization, PeQD-based photovoltaics are well-positioned to make a meaningful contribution to the future of renewable energy.

Author contributions

Y. Xu prepared the manuscript under the guidance of Q. Yu. X. Zhang and C. Zhu discussed and co-edited the manuscript.

Conflicts of interest

The authors declare no conflict of interest.

Data availability

No primary research results, software or code have been included and no new data were generated or analysed as part of this review.

Acknowledgements

The authors acknowledge the financial support from NSF ECCS-2054942, ECCS-2404675, and DMR-2114350.

References

1 P. Zhu, C. Chen, J. Dai, Y. Zhang, R. Mao, S. Chen, J. Huang and J. Zhu, *Adv. Mater.*, 2024, **36**, 2307357.
2 J. Y. Kim, J.-W. Lee, H. S. Jung, H. Shin and N.-G. Park, *Chem. Rev.*, 2020, **120**, 7867–7918.
3 W.-J. Yin, J.-H. Yang, J. Kang, Y. Yan and S.-H. Wei, *J. Mater. Chem. A*, 2015, **3**, 8926–8942.
4 J. Y. Jiang, *Prog. Photovoltaics Res. Appl.*, 2025, **33**, 795–810.
5 Q. Dong, Y. Fang, Y. Shao, P. Mulligan, J. Qiu, L. Cao and J. Huang, *Science*, 2015, **347**, 967–970.
6 Y. Chen, H. Yi, X. Wu, R. Haroldson, Y. Gartstein, Y. Rodionov, K. Tikhonov, A. Zakhidov, X.-Y. Zhu and V. Podzorov, *Nat. Commun.*, 2016, **7**, 12253.
7 R. Prasanna, A. Gold-Parker, T. Leijtens, B. Conings, A. Babayigit, H.-G. Boyen, M. F. Toney and M. D. McGehee, *J. Am. Chem. Soc.*, 2017, **139**, 11117–11124.
8 A. Miyata, A. Mitioglu, P. Plochocka, O. Portugall, J. T.-W. Wang, S. D. Stranks, H. J. Snaith and R. J. Nicholas, *Nat. Phys.*, 2015, **11**, 582–587.
9 H. Zhu, S. Teale, M. N. Lintangpradipto, S. Mahesh, B. Chen, M. D. McGehee, E. H. Sargent and O. M. Bakr, *Nat. Rev. Mater.*, 2023, **8**, 569–586.
10 C. C. Boyd, R. Cheacharoen, T. Leijtens and M. D. McGehee, *Chem. Rev.*, 2018, **119**, 3418–3451.
11 Q. A. Akkerman, G. Rainò, M. V. Kovalenko and L. Manna, *Nat. Mater.*, 2018, **17**, 394–405.
12 H. Huang, M. I. Bodnarchuk, S. V. Kershaw, M. V. Kovalenko and A. L. Rogach, *ACS Energy Lett.*, 2017, **2**, 2071–2083.
13 J. Shamsi, A. S. Urban, M. Imran, L. De Trizio and L. Manna, *Chem. Rev.*, 2019, **119**, 3296–3348.
14 F. Haydous, J. M. Gardner and U. B. Cappel, *J. Mater. Chem. A*, 2021, **9**, 23419–23443.
15 C. Wei, W. Su, J. Li, B. Xu, Q. Shan, Y. Wu, F. Zhang, M. Luo, H. Xiang and Z. Cui, *Adv. Mater.*, 2022, **34**, 2107798.
16 X. Zhang, H. Huang, C. Zhao, L. Jin, C. Lee, Y. Li, D.-H. Ko, W. Ma, T. Wu and J. Yuan, *Nat. Energy*, 2024, 1–10.
17 J. Yuan, C. Bi, S. Wang, R. Guo, T. Shen, L. Zhang and J. Tian, *Adv. Funct. Mater.*, 2019, **29**, 1906615.
18 A. Swarnkar, A. R. Marshall, E. M. Sanehira, B. D. Chernomordik, D. T. Moore, J. A. Christians, T. Chakrabarti and J. M. Luther, *Science*, 2016, **354**, 92–95.
19 E. M. Sanehira, A. R. Marshall, J. A. Christians, S. P. Harvey, P. N. Ciesielski, L. M. Wheeler, P. Schulz, L. Y. Lin, M. C. Beard and J. M. Luther, *Sci. Adv.*, 2017, **3**, eaao4204.
20 H. Aqoma, S.-H. Lee, I. F. Imran, J.-H. Hwang, S.-H. Lee and S.-Y. Jang, *Nat. Energy*, 2024, **9**, 324–332.
21 L. Protesescu, S. Yakunin, M. I. Bodnarchuk, F. Krieg, R. Caputo, C. H. Hendon, R. X. Yang, A. Walsh and M. V. Kovalenko, *Nano Lett.*, 2015, **15**, 3692–3696.
22 Y. Yuan and J. Huang, *Acc. Chem. Res.*, 2016, **49**, 286–293.
23 E. T. Hoke, D. J. Slotcavage, E. R. Dohner, A. R. Bowring, H. I. Karunadasa and M. D. McGehee, *Chem. Sci.*, 2015, **6**, 613–617.
24 A. J. Barker, A. Sadhanala, F. Deschler, M. Gandini, S. P. Senanayak, P. M. Pearce, E. Mosconi, A. J. Pearson, Y. Wu and A. R. Srimath Kandada, *ACS Energy Lett.*, 2017, **2**, 1416–1424.
25 A. J. Knight, A. D. Wright, J. B. Patel, D. P. McMeekin, H. J. Snaith, M. B. Johnston and L. M. Herz, *ACS Energy Lett.*, 2018, **4**, 75–84.
26 K. Sakhatskyi, R. A. John, A. Guerrero, S. Tsarev, S. Sabisch, T. Das, G. J. Matt, S. Yakunin, I. Cherniukh and M. Kotyrba, *ACS Energy Lett.*, 2022, **7**, 3401–3414.
27 D. Meggiolaro, E. Mosconi and F. De Angelis, *ACS Energy Lett.*, 2019, **4**, 779–785.
28 G. Nedelcu, L. Protesescu, S. Yakunin, M. I. Bodnarchuk, M. J. Grotevent and M. V. Kovalenko, *Nano Lett.*, 2015, **15**, 5635–5640.

29 Q. A. Akkerman, V. D'innocenzo, S. Accornero, A. Scarpellini, A. Petrozza, M. Prato and L. Manna, *J. Am. Chem. Soc.*, 2015, **137**, 10276–10281.
30 Z. Li, M. Yang, J.-S. Park, S.-H. Wei, J. J. Berry and K. Zhu, *Chem. Mater.*, 2016, **28**, 284–292.
31 S. Li, Y. Jiang, J. Xu, D. Wang, Z. Ding, T. Zhu, B. Chen, Y. Yang, M. Wei and R. Guo, *Nature*, 2024, **635**, 82–88.
32 S. Masi, A. F. Gualdrón-Reyes and I. Mora-Sero, *ACS Energy Lett.*, 2020, **5**, 1974–1985.
33 J. A. Steele, H. Jin, I. Dovgaliuk, R. F. Berger, T. Braeckevelt, H. Yuan, C. Martin, E. Solano, K. Lejaeghere and S. M. Rogge, *Science*, 2019, **365**, 679–684.
34 J. A. Vigil, A. Hazarika, J. M. Luther and M. F. Toney, *ACS Energy Lett.*, 2020, **5**, 2475–2482.
35 A. Hazarika, Q. Zhao, E. A. Gaulding, J. A. Christians, B. Dou, A. R. Marshall, T. Moot, J. J. Berry, J. C. Johnson and J. M. Luther, *ACS Nano*, 2018, **12**, 10327–10337.
36 J. Kim, Y. Xu, D. Bain, M. Li, M. Cotlet, Q. Yu and A. J. Musser, *ACS Nano*, 2023, **17**, 23079–23093.
37 P. Caprioglio, M. Stolterfoht, C. M. Wolff, T. Unold, B. Rech, S. Albrecht and D. Neher, *Adv. Energy Mater.*, 2019, **9**, 1901631.
38 J. Warby, S. Shah, J. Thiesbrummel, E. Gutierrez-Partida, H. Lai, B. Alebachew, M. Grischek, F. Yang, F. Lang and S. Albrecht, *Adv. Energy Mater.*, 2023, **13**, 2303135.
39 B. M. Wieliczka, J. A. Márquez, A. M. Bothwell, Q. Zhao, T. Moot, K. T. VanSant, A. J. Ferguson, T. Unold, D. Kuciauskas and J. M. Luther, *ACS Nano*, 2021, **15**, 19334–19344.
40 L. Hu, X. Guan, H. Huang, T. Ye, J. Ding, A. Aarti, K. Venkatesan, W. Wang, F. Chen and C.-H. Lin, *ACS Energy Lett.*, 2024, **9**, 3970–3981.
41 Q. Zhao, A. Hazarika, X. Chen, S. P. Harvey, B. W. Larson, G. R. Teeter, J. Liu, T. Song, C. Xiao and L. Shaw, *Nat. Commun.*, 2019, **10**, 2842.
42 F. Li, S. Zhou, J. Yuan, C. Qin, Y. Yang, J. Shi, X. Ling, Y. Li and W. Ma, *ACS Energy Lett.*, 2019, **4**, 2571–2578.
43 L. Protesescu, S. Yakunin, M. I. Bodnarchuk, F. Bertolotti, N. Masciocchi, A. Guagliardi and M. V. Kovalenko, *J. Am. Chem. Soc.*, 2016, **138**, 14202–14205.
44 L. Protesescu, S. Yakunin, S. Kumar, J. Bär, F. Bertolotti, N. Masciocchi, A. Guagliardi, M. Grotevent, I. Shorubalko and M. I. Bodnarchuk, *ACS Nano*, 2017, **11**, 3119–3134.
45 Y. Cai, H. Wang, Y. Li, L. Wang, Y. Lv, X. Yang and R.-J. Xie, *Chem. Mater.*, 2019, **31**, 881–889.
46 J. Chen, D. Jia, R. Zhuang, Y. Hua and X. Zhang, *Adv. Mater.*, 2022, **34**, 2204259.
47 S. Ding, M. Hao, C. Fu, T. Lin, A. Baktash, P. Chen, D. He, C. Zhang, W. Chen and A. K. Whittaker, *Adv. Sci.*, 2022, **9**, 2204476.
48 J. Shi, B. Cohen-Kleinstein, X. Zhang, C. Zhao, Y. Zhang, X. Ling, J. Guo, D.-H. Ko, B. Xu and J. Yuan, *Nano-Micro Lett.*, 2023, **15**, 163.
49 C. B. Whitehead, S. Özkar and R. G. Finke, *Mater. Adv.*, 2021, **2**, 186–235.
50 Y. Dong, T. Qiao, D. Kim, D. Parobek, D. Rossi and D. H. Son, *Nano Lett.*, 2018, **18**, 3716–3722.
51 L. Zhang, C. Kang, G. Zhang, Z. Pan, Z. Huang, S. Xu, H. Rao, H. Liu, S. Wu and X. Wu, *Adv. Funct. Mater.*, 2021, **31**, 2005930.
52 M. Imran, V. Caligiuri, M. Wang, L. Goldoni, M. Prato, R. Krahne, L. De Trizio and L. Manna, *J. Am. Chem. Soc.*, 2018, **140**, 2656–2664.
53 Y. Qian, Y. Shi, G. Shi, G. Shi, X. Zhang, L. Yuan, Q. Zhong, Y. Liu, Y. Wang and X. Ling, *Sol. RRL*, 2021, **5**, 2100090.
54 P. Liu, W. Chen, W. Wang, B. Xu, D. Wu, J. Hao, W. Cao, F. Fang, Y. Li and Y. Zeng, *Chem. Mater.*, 2017, **29**, 5168–5173.
55 A. Dutta, R. K. Behera, P. Pal, S. Baitalik and N. Pradhan, *Angew. Chem., Int. Ed.*, 2019, **58**, 5552–5556.
56 Y. Bai, M. Hao, S. Ding, P. Chen and L. Wang, *Adv. Mater.*, 2022, **34**, 2105958.
57 D. Jia, J. Chen, X. Mei, W. Fan, S. Luo, M. Yu, J. Liu and X. Zhang, *Energy Environ. Sci.*, 2021, **14**, 4599–4609.
58 F. Li, X. Zhang, J. Shi, L. Jin, J. Qiao, J. Guo, H. Yin, Y. Li, J. Yuan and W. Ma, *Adv. Funct. Mater.*, 2023, **33**, 2302542.
59 J. Leemans, K. C. Dumbgen, M. M. Minjauw, Q. Zhao, A. Vantomme, I. Infante, C. Detavernier and Z. Hens, *J. Am. Chem. Soc.*, 2021, **143**, 4290–4301.
60 X. Zhang, H. Huang, Y. M. Maung, J. Yuan and W. Ma, *Chem. Commun.*, 2021, **57**, 7906–7909.
61 E. T. Vickers, T. A. Graham, A. H. Chowdhury, B. Bahrami, B. W. Dreskin, S. Lindley, S. B. Naghadeh, Q. Qiao and J. Z. Zhang, *ACS Energy Lett.*, 2018, **3**, 2931–2939.
62 E. T. Vickers, E. E. Enlow, W. G. Delmas, A. C. DiBenedetto, A. H. Chowdhury, B. Bahrami, B. W. Dreskin, T. A. Graham, I. N. Hernandez and S. A. Carter, *ACS Energy Lett.*, 2020, **5**, 817–825.
63 H. Huang, X. Zhang, R. Gui, C. Zhao, J. Guo, Y. M. Maung, H. Yin, W. Ma and J. Yuan, *Adv. Funct. Mater.*, 2023, **33**, 2210728.
64 C. Zhao, J. Shi, H. Huang, Q. Zhao, X. Zhang and J. Yuan, *Small Sci.*, 2024, **4**, 2300132.
65 W. Yang, S. H. Jo, Y. Tang, J. Park, S. G. Ji, S. H. Cho, Y. Hong, D. H. Kim, J. Park and E. Yoon, *Adv. Mater.*, 2023, **35**, 2304533.
66 M. Hao, Y. Bai, S. Zeiske, L. Ren, J. Liu, Y. Yuan, N. Zarrabi, N. Cheng, M. Ghasemi and P. Chen, *Nat. Energy*, 2020, **5**, 79–88.
67 C. Zhao, X. Zhang, H. Huang and J. Yuan, *J. Chem. Phys.*, 2022, **157**(3), 031101.
68 C. Zhao, C. Cazorla, X. Zhang, H. Huang, X. Zhao, D. Li, J. Shi, Q. Zhao, W. Ma and J. Yuan, *J. Am. Chem. Soc.*, 2024, **146**, 4913–4921.
69 D. Jia, J. Chen, R. Zhuang, Y. Hua and X. Zhang, *Adv. Mater.*, 2023, **35**, 2212160.
70 G. Wang, Y. Sun, X. Mei, M. Zhang, J. Qiu, Z. Sun and X. Zhang, *Angew. Chem., Int. Ed.*, 2024, e202416747.
71 J. Shi, F. Li, J. Yuan, X. Ling, S. Zhou, Y. Qian and W. Ma, *J. Mater. Chem. A*, 2019, **7**, 20936–20944.
72 J. Hallstrom, I. Cherniukh, X. Zha, M. V. Kovalenko and A. Travesset, *ACS Nano*, 2023, **17**, 7219–7228.
73 Y. Xu, H. Li, S. Ramakrishnan, D. Song, Y. Zhang, M. Cotlet and Q. Yu, *ACS Appl. Energy Mater.*, 2022, **5**, 9858–9869.

74 S. Jeon, M.-C. Jung, J. Ahn, H. K. Woo, J. Bang, D. Kim, S. Y. Lee, H. Y. Woo, J. Jeon and M. J. Han, *Nanoscale Horiz.*, 2020, **5**, 960–970.
75 D. Jia, J. Chen, R. Zhuang, Y. Hua and X. Zhang, *Energy Environ. Sci.*, 2022, **15**, 4201–4212.
76 L. M. Wheeler, E. M. Sanehira, A. R. Marshall, P. Schulz, M. Suri, N. C. Anderson, J. A. Christians, D. Nordlund, D. Sokaras and T. Kroll, *J. Am. Chem. Soc.*, 2018, **140**, 10504–10513.
77 S. B. Shivarudraiah, M. Ng, C.-H. A. Li and J. E. Halpert, *ACS Appl. Energy Mater.*, 2020, **3**, 5620–5627.
78 D. Jia, J. Chen, J. Qiu, H. Ma, M. Yu, J. Liu and X. Zhang, *Joule*, 2022, **6**, 1632–1653.
79 X. Zhang, H. Huang, L. Jin, C. Wen, Q. Zhao, C. Zhao, J. Guo, C. Cheng, H. Wang and L. Zhang, *Angew. Chem., Int. Ed.*, 2023, **62**, e202214241.
80 S. Rühle, *Sol. Energy*, 2016, **130**, 139–147.
81 M. Kim, G.-H. Kim, T. K. Lee, I. W. Choi, H. W. Choi, Y. Jo, Y. J. Yoon, J. W. Kim, J. Lee and D. Huh, *Joule*, 2019, **3**, 2179–2192.
82 D. Jia, J. Chen, M. Yu, J. Liu, E. M. Johansson, A. Hagfeldt and X. Zhang, *Small*, 2020, **16**, 2001772.
83 M. Que, H. Yuan, Q. Wu, S. He, P. Zhong and B. Li, *ACS Appl. Mater. Interfaces*, 2024, **16**, 6189–6197.
84 Y. Wang, J. Yuan, X. Zhang, X. Ling, B. W. Larson, Q. Zhao, Y. Yang, Y. Shi, J. M. Luther and W. Ma, *Adv. Mater.*, 2020, **32**, 2000449.
85 S. Ding, J. A. Steele, P. Chen, T. Lin, D. He, C. Zhang, X. Fan, E. Solano, A. K. Whittaker and M. Hao, *Adv. Energy Mater.*, 2023, **13**, 2301817.
86 Q. Jiang, J. Tong, Y. Xian, R. A. Kerner, S. P. Dunfield, C. Xiao, R. A. Scheidt, D. Kuciauskas, X. Wang and M. P. Hautzinger, *Nature*, 2022, **611**, 278–283.
87 X. Ling, J. Yuan, X. Zhang, Y. Qian, S. M. Zakeeruddin, B. W. Larson, Q. Zhao, J. Shi, J. Yang and K. Ji, *Adv. Mater.*, 2020, **32**, 2001906.
88 M. Li, Y. Bao, W. Hui, K. Sun, L. Gu, X. Kang, D. Wang, B. Wang, H. Deng and R. Guo, *Adv. Mater.*, 2024, **36**, 2309890.
89 L. Hu, Q. Zhao, S. Huang, J. Zheng, X. Guan, R. Patterson, J. Kim, L. Shi, C.-H. Lin and Q. Lei, *Nat. Commun.*, 2021, **12**, 466.
90 K. Ji, J. Yuan, F. Li, Y. Shi, X. Ling, X. Zhang, Y. Zhang, H. Lu, J. Yuan and W. Ma, *J. Mater. Chem. A*, 2020, **8**, 8104–8112.
91 R. Han, L. Duan, Y. Xu, L. Kong, G. Liu, J. Ni and J. Zhang, *ACS Appl. Mater. Interfaces*, 2024, **16**, 69459–69466.
92 J. Xue, R. Wang, L. Chen, S. Nuryyeva, T. H. Han, T. Huang, S. Tan, J. Zhu, M. Wang and Z. K. Wang, *Adv. Mater.*, 2019, **31**, 1900111.
93 J. Yuan, X. Zhang, J. Sun, R. Patterson, H. Yao, D. Xue, Y. Wang, K. Ji, L. Hu and S. Huang, *Adv. Funct. Mater.*, 2021, **31**, 2101272.
94 S. Li, Z. Wang, Y. Li, C.-J. Su, Y. Fu, Y. Wang and X. Lu, *ACS Nano*, 2023, **17**, 20634–20642.
95 Q. A. Akkerman, T. P. Nguyen, S. C. Boehme, F. Montanarella, D. N. Dirin, P. Wechsler, F. Beiglböck, G. Rainò, R. Erni and C. Katan, *Science*, 2022, **377**, 1406–1412.
96 F. Montanarella, Q. A. Akkerman, D. Bonatz, M. M. van der Sluijs, J. C. van der Bok, P. T. Prins, M. Aebli, A. Mews, D. Vanmaekelbergh and M. V. Kovalenko, *Nano Lett.*, 2023, **23**, 667–676.
97 I. Lignos, S. Stavrakis, G. Nedelcu, L. Protesescu, A. J. Demello and M. V. Kovalenko, *Nano Lett.*, 2016, **16**, 1869–1877.
98 K. Abdel-Latif, R. W. Epps, C. B. Kerr, C. M. Papa, F. N. Castellano and M. Abolhasani, *Adv. Funct. Mater.*, 2019, **29**, 1900712.
99 Y. Dong, Y.-K. Wang, F. Yuan, A. Johnston, Y. Liu, D. Ma, M.-J. Choi, B. Chen, M. Chekini and S.-W. Baek, *Nat. Nanotechnol.*, 2020, **15**, 668–674.
100 J. Chen, D. Jia, J. Qiu, R. Zhuang, Y. Hua and X. Zhang, *Nano Energy*, 2022, **96**, 107140.
101 H. Huang, X. Zhang, C. Zhao and J. Yuan, *Mater. Chem. Front.*, 2023, **7**, 1423–1430.
102 S. Wang, Q. Zhao, A. Hazarika, S. Li, Y. Wu, Y. Zhai, X. Chen, J. M. Luther and G. Li, *Nat. Commun.*, 2023, **14**, 2216.
103 C. J. Thomas, Y. Zhang, A. Guillaussier, K. Bdeir, O. F. Aly, H. G. Kim, J. Noh, L. C. Reimnitz, J. Li and F. L. Deepak, *Chem. Mater.*, 2019, **31**, 9750–9758.
104 S. Wang, Z. Huang, X. Wang, Y. Li, M. Günther, S. Valenzuela, P. Parikh, A. Cabreros, W. Xiong and Y. S. Meng, *J. Am. Chem. Soc.*, 2018, **140**, 16720–16730.
105 F. M. Rombach, S. A. Haque and T. J. Macdonald, *Energy Environ. Sci.*, 2021, **14**, 5161–5190.
106 Q. Fu, X. Tang, H. Liu, R. Wang, T. Liu, Z. Wu, H. Y. Woo, T. Zhou, X. Wan and Y. Chen, *J. Am. Chem. Soc.*, 2022, **144**, 9500–9509.
107 X. Zhang, X. Liu, F. F. Tirani, B. Ding, J. Chen, G. Rahim, M. Han, K. Zhang, Y. Zhou and H. Quan, *Angew. Chem.*, 2024, **136**, e202320152.
108 B. Dong, M. Wei, Y. Li, Y. Yang, W. Ma, Y. Zhang, Y. Ran, M. Cui, Z. Su and Q. Fan, *Nat. Energy*, 2025, **10**, 342–353.
109 Q. Jiang and K. Zhu, *Nat. Rev. Mater.*, 2024, **9**, 399–419.
110 H. Li, H. Huang, D. Li, X. Zhang, C. Zhao, X. Zhao, W. Ma and J. Yuan, *Energy Environ. Sci.*, 2025, **18**, 972–981.